




**Exciton-exciton transitions involving strongly bound excitons: An *ab initio* approach**D. Sangalli <sup>1</sup>, M. D'Alessandro <sup>2</sup>, and C. Attaccalite <sup>3</sup><sup>1</sup>*Istituto di Struttura della Materia-CNR (ISM-CNR), Area della Ricerca di Roma 1, Monterotondo Scalo, Italy*<sup>2</sup>*Istituto di Struttura della Materia-CNR (ISM-CNR), Via del Fosso del Cavaliere 100, 00133 Roma, Italia*<sup>3</sup>*CNRS/Mix-Marseille Université, Centre Interdisciplinaire de Nanoscience de Marseille UMR 7325 Campus de Luminy, 13288 Marseille Cedex 9, France*

(Received 22 November 2022; revised 15 April 2023; accepted 17 April 2023; published 15 May 2023)

In pump-probe spectroscopy, two laser pulses are employed to garner dynamical information from the sample of interest. The pump initiates the optical process by exciting a portion of the sample from the electronic ground state to an accessible electronic excited state, an exciton. Thereafter, the probe interacts with the already excited sample. The change in the absorbance after the pump provides information on transitions between the excited states and their dynamics. In this work, we study these exciton-exciton transitions by means of an *ab initio* real-time propagation scheme based on dynamical Berry phase formulation. The results are then analyzed taking advantage of a Fermi golden rule approach formulated in the excitonic basis-set and in terms of the symmetries of the excitonic states. Using bulk LiF and two-dimensional hBN as two prototype materials, we discuss the selection rules for transitions involving strongly bound Frenkel excitons, for which the hydrogen model cannot be used.

DOI: [10.1103/PhysRevB.107.205203](https://doi.org/10.1103/PhysRevB.107.205203)**I. INTRODUCTION**

Excitons are composite particles formed by bound electron-hole (eh) pairs. Optically bright excitons dominate the equilibrium absorption spectrum of a wide class of materials, and they can be easily measured [1]. While in standard semiconductors their binding energy is of a few meV, in other systems such as two-dimensional (2D) materials [2], insulators such as LiF and hBN [3–7], semiconductors such as Cu<sub>2</sub>O [8] or BiI<sub>3</sub> [9,10], or in organic semiconductors [11,12], it can be as high as hundreds of meV, making excitons stable at room temperature. As a consequence, optically injected excitons can be exploited for optoelectronic devices [13]. This calls for a detailed understanding of the excitonic properties and their dynamics.

Different phenomena can participate in the exciton dynamics. Excitons can scatter with defects, phonons, annihilate each other (Auger effect), or end up in dark states [14–19], and the knowledge of these state is crucial to predict the dynamics. However, while bright excitons can be easily investigated both experimentally and theoretically, dark excitons are much more difficult to measure. The validation of numerical modeling can often be achieved only in a very indirect way, via accurate comparison between numerical simulations and experimental measurements. Time-resolved angle-resolved photoemission (TR-ARPES) measurements can be used to measure both dark and bright excitons [20,21]. However, TR-ARPES experiments require a complex experimental setup, they often have limited energy resolution, and they are restrained to the study of the lowest energy excitons [22,23]. Two possible setups to directly investigate dark excitons via table-top absorption are nonlinear optics experiments at equilibrium, and transient absorption (TR-abs) experiments in the nonequilibrium regime. In the nonlinear regime, two-photon absorption has been used to directly excite dark excitons in 2D [24–26] and 1D [27]

materials, and accurate schemes based on *ab initio* simulations have been developed to describe these experiments [28]. In the nonequilibrium regime, dark excitons can be explored via TR-Abs by combining optical and THz (or infrared) laser pulses. A first optical pump pulse is used, with frequency tuned resonant to some excitonic peak, and a second THz probe pulse is used to measure transitions from the initially injected bright exciton towards available dark excitons. This was explored, for example, in GaAs quantum wells [29,30], in bulk silicon [31,32], and in materials with larger excitonic binding energy, such as Cu<sub>2</sub>O [33], 2D layers [34–37], and hybrid organic-inorganic semiconductors [38]. However, no *ab initio* approach has been developed so far to model these experiments.

Exciton-to-exciton transitions are usually divided into two groups: (i) interexciton transitions, if the initial and final state belong to two different excitonic series, or (ii) intraexciton transitions, if the initial and final state belong to the same excitonic series. This nomenclature reflects the state of the art in modeling these experiments, which is largely based on the hydrogen model for the exciton, which assumes a rotational invariant Hamiltonian, and labels the excitonic states as  $1s$ ,  $2s$ ,  $2p$ , i.e., in terms of the principal quantum number and the angular momentum. The hydrogen model can be accurate for Wannier excitons, but it needs to be integrated with approaches that account for the underlying symmetries and/or topology of the band structure. Moreover, it may fail in systems with Frenkel-like excitons, where the exciton wave functions are strongly affected by the lattice symmetry [7], and they do not follow the standard hydrogen series. It is important here to underline that strongly bound excitons, which are stable at room temperature, are usually more Frenkel-like than Wannier-like, but that often an exact distinction between these two kinds of excitons cannot be made.

For these reasons, in this manuscript we propose a fully *ab initio* approach to the study of pump and probe (P&P) spectroscopy, which includes both inter- and intraexciton transitions on an equal footing and takes fully into account lattice symmetries. We apply this approach to the case of a strong pump and a test probe in such a way as to compare the results with a perturbative approach based on quasiequilibrium response theory. However, we expect that real-time propagation could be used beyond this regime also including pump-probe interference and dephasing effects, which at present are not included in our approach.

Since two laser pulses are involved, TR-Abs can be described as a nonlinear response of the material under the action of both the pump and the probe laser pulses, and an approach similar to the one developed to model two-photon absorption could be used. The signal reconstructed by computing a nonlinear response function is, by construction, perturbative in the effect of the pump pulse. Furthermore, the approach can only be used to describe the situation in which the probe detects the state directly generated by the pump, while it cannot deal with states generated by subsequent relaxation processes. In this situation, the physics of TR-Abs is very similar to that of equilibrium nonlinear response experiments. Extending nonlinear response theory beyond this regime becomes very cumbersome [39]. As an alternative, one can compute (or guess) the nonequilibrium state created by the pump pulse and/or by the subsequent dynamics, and compute the nonequilibrium linear response with respect to the probe pulse. In this second approach, the pump pulse can be considered in a nonperturbative way, and deviations from the ideal excitonic picture can be computed. More importantly, the approach holds beyond the overlap regime. This angle clearly shows that TR-Abs experiments can access much more information if compared to equilibrium nonlinear optics experiments. Due to the action of relaxation processes, the initially generated bright excitonic state can be sent into other dark excitonic states (also including finite momentum excitons). Thus both exciton-to-exciton transitions involving finite momentum excitons, and exciton dynamics can be probed in a TR-abs setup.

In the present manuscript we follow the second approach outlined above, and we employ a real-time propagation scheme based on an effective Schrödinger equation where correlation effects has been derived from Green's function theory [40,41]. In the equation of motion (EOM), the coupling term for the external field is constructed via the nonequilibrium Berry phase theory, where both the pump and the probe laser pulses are included [42]. This analysis does not rely on any excitonic basis set, and the excitonic state created by the pump pulse naturally emerges from the inclusion of the many-body self-energy. Moreover, in order to analyze the results obtained via the explicit real-time propagation scheme for the THz/infrared response function, we employ an alternative Fermi golden rule approach in the excitonic basis set. In this latter case, instead of computing the nonequilibrium state, we assume it can be described in terms of a well-defined excitonic eigenstate obtained from the solution of the Bethe-Salpeter equation (BSE) [43]. A similar approach has already been used in the study of the second-harmonic response with very good results [44]. Moreover, the explicit use of an excitonic

basis set allows us to analyze the symmetries of the excitonic wave functions and use them to identify the dipole-allowed exciton-exciton transitions, with an approach that generalizes the standard hydrogen model. While this approach holds in the low-intensity limit, it also offers a starting point to describe the deviation from the ideal excitonic picture, in terms of renormalization of the excitonic energies and wave functions.

We investigate two materials: bulk lithium fluoride (LiF) and monolayer hexagonal boron nitrite (hBN). LiF belongs to the family of alkali halides, and it has been investigated in many theoretical and computational papers as a prototype material hosting tightly bound excitons [4,45–52]. hBN, on the other hand, is a layered insulator that in recent years has found many applications as a substrate and as a light emitter in the ultraviolet [53]. From the theoretical point of view it has been extensively studied with both tight-binding models and *ab initio* calculations [7], also including an accurate comparison with the hydrogen model labeling for the excitonic states.

The manuscript is organized as follows: in Sec. II we describe the theory for the real-time simulation, the Fermi golden rule approach, and the selection rules that enter in the pump and probe spectroscopy; in Sec. III we present P&P response for LiF and hBN and we discuss its interpretation; finally, in Sec. IV we draw conclusions and discuss perspectives from the theoretical and experimental points of view of P&P techniques.

## II. THEORY

This section is divided into three parts. In Sec. II A we put forward the formalism to compute the exciton-exciton transition. It is based on the nonequilibrium Berry phase theory. The formalism holds at any exciton density, while the approximation we use for the self-energy, in particular the equilibrium screening approximation, limits the approach to a regime where the nonequilibrium screening can be neglected, i.e., below the exciton-Mott transition. Within this limit, corrections to the spectra due to the increasing exciton density could be computed. Then in Sec. II B we discuss a simplified approach, based on the Fermi golden rule in the excitonic basis set. This latter requires an initial guess for the many-body state generated by the pump pulse, and it holds only for low exciton densities. Starting from this, in Sec. II C, we analyze the dipole-allowed exciton-to-exciton transitions both in terms of the coefficients of the exciton wave functions and taking advantage of group theory, starting from the point group associated with the crystal structure of the material.

### A. Real-time propagation

In the real-time simulations, the response of the system is obtained from the equations of motion for the valence-band states:

$$i\hbar \frac{d}{dt} |v_{m\mathbf{k}}(t)\rangle = [H_{\mathbf{k}}^{\text{MB}} + iU^{\text{ext}}(t)] |v_{m\mathbf{k}}(t)\rangle, \quad (1)$$

where  $|v_{m\mathbf{k}}(t)\rangle$  is the periodic part of the occupied (at equilibrium) Bloch states. In the right-hand side (r.h.s.) of Eq. (1),  $H_{\mathbf{k}}^{\text{MB}}$  is the effective Hamiltonian derived from many-body theory [40]. To catch excitonic effects in the real-time

dynamics, we choose a many-body Hamiltonian  $H_{\mathbf{k}}^{\text{MB}}$  in the form

$$H_{\mathbf{k}}^{\text{MB}} \equiv H_{\mathbf{k}}^{\text{KS}} + \Delta H_{\mathbf{k}} + \Delta \Sigma^{\text{HSEX}}[\rho(t)]. \quad (2)$$

The unperturbed (zero-field) Hamiltonian is constructed starting from the Kohn-Sham term,  $H_{\mathbf{k}}^{\text{KS}}$  [54], and it includes the equilibrium quasiparticle corrections  $\Delta H_{\mathbf{k}}$ . The term  $\Delta \Sigma^{\text{HSEX}} = \Sigma^{\text{HSEX}}[\rho(t)] - \Sigma^{\text{HSEX}}[\rho(0)]$  depends on the time-dependent electronic density-matrix  $\rho(t)$ , which can be reconstructed in the equilibrium basis set  $|v_{n\mathbf{k}}(0)\rangle$  from the time-dependent valence states as

$$\rho_{nm\mathbf{k}}(t) = \sum_{n' \in \text{occ}} \langle v_{n\mathbf{k}}(0) | v_{n'\mathbf{k}}(t) \rangle \langle v_{n'\mathbf{k}}(t) | v_{m\mathbf{k}}(0) \rangle, \quad (3)$$

where the sum runs over the occupied states only.  $\Delta \Sigma_{\text{HSEX}}$  describes the update, during the real-time propagation, of the Hartree (H) term, responsible for the local-field effects, plus of the Screened-EXchange (SEX) self-energy, that accounts for the electron-hole interaction and excitonic effect [43].

The real-time propagation with the above Hamiltonian corresponds to a time-dependent (TD) version of the Bethe-Salpeter equation, and it is also known in the literature as TD-HSEX. Indeed, in the limit of small perturbation (i.e., in the linear regime) these equations reproduce the optical absorption calculated with the standard  $G_0W_0 + \text{BSE}$  approach, as shown in Ref. [40]. Equation (3) also shows how the EOM for the valence wave functions, e.g., Eq. (1), relates to the scheme using the EOM for the density matrix [40]. In fact, while only valence block states are propagated in Eq. (1),  $\rho_{nm\mathbf{k}}$  is expanded in a Kohn-Sham basis set, namely in terms of valence and conduction bands. Therefore, the number of conduction bands must be converged in both schemes [55]. However, knowing the time-dependent wave function gives access to more information, and it allows the calculation of the Berry polarization, as discussed below.

In the linear regime (and for nonferroelectric materials), a closed EOM can be written by expressing the coupling with the external field  $U^{\text{ext}}(t) = \mathcal{E}(t) \cdot \hat{\mathbf{P}}^{(1)}$ , via the first-order polarization operator  $\hat{\mathbf{P}}^{(1)}$  written in the KS basis set in terms of the transition dipoles  $\mathbf{r}_{nm\mathbf{k}}$ , e.g.,  $P_{nm\mathbf{k}}^{(1)} = -e\mathbf{r}_{nm\mathbf{k}}$ . The expectation value of such an operator gives the macroscopic polarization:

$$\mathbf{P}^{(1)} = -e \sum_{nm\mathbf{k}} \tilde{\mathbf{r}}_{nm\mathbf{k}} \rho_{nm\mathbf{k}}, \quad (4)$$

where the  $\sim$  on the sum means that all terms for which  $|\epsilon_{n\mathbf{k}} - \epsilon_{m\mathbf{k}}| < \epsilon_{\text{thresh}}$  are neglected, since  $\hat{P}_{nm\mathbf{k}}^{(1)}$  is not defined for those terms. Here  $\epsilon_{n\mathbf{k}}$  are the eigenvalues of  $H_{\mathbf{k}}^{\text{KS}}$  at equilibrium, and  $\epsilon_{\text{thresh}} = 10^{-5}$  eV (see also related discussion in Sec. II B). However, in the present case we need to probe the response to the system after the action of the pump, and we thus need to go beyond this first-order approach. This can be achieved by means of the Berry phase formulation, e.g., by defining the coupling with the external field as  $U^{\text{ext}}(t) = \mathcal{E}(t) \cdot \tilde{\delta}_{\mathbf{k}}$ , which holds to all orders. As we imposed Born-von Kármán periodic boundary conditions, the coupling takes the form of a  $\mathbf{k}$ -derivative operator  $\tilde{\delta}_{\mathbf{k}}$ . The tilde indicates that the operator is ‘‘gauge-covariant’’ and guarantees that the solutions of Eq. (1) are invariant under unitary rotations among occupied states at  $\mathbf{k}$  (see Ref. [42] for more details). This derivative is calculated using a finite-difference five-point midpoint formula [56].

From the evolution of  $|v_{m\mathbf{k}}\rangle$  in Eq. (1), we calculate the real-time polarization  $\mathbf{P}_{\mathbf{a}_i}$  along the lattice vector  $\mathbf{a}_i$  as

$$\mathbf{P}_{\mathbf{a}_i} = -\frac{ef|\mathbf{a}_i|}{2\pi\Omega_c} \text{Im} \ln \prod_{\mathbf{k}}^{N_{\mathbf{k}}-1} \det S(\mathbf{k}, \mathbf{k} + \mathbf{q}_i), \quad (5)$$

where  $S(\mathbf{k}, \mathbf{k} + \mathbf{q}_i)$  is the overlap matrix between the valence states  $|v_{n\mathbf{k}}\rangle$  and  $|v_{m\mathbf{k}+\mathbf{q}_i}\rangle$ ,  $\Omega_c$  is the unit-cell volume,  $f$  is the spin degeneracy,  $N_{\mathbf{k}}$  is the number of  $\mathbf{k}$  points along the polarization direction, and  $|\mathbf{q}_i| = 2\pi/(N_{\mathbf{k}}|\mathbf{a}_i|)$ . Equation (5) is the adiabatic extension to the nonequilibrium regime of the definition of the polarization in an extended system [42].

Via the solution of Eq. (1), the transient absorption signal is finally defined as the Fourier transform of

$$\Delta \mathbf{P}(t) = \mathbf{P}_{pp}(t) - \mathbf{P}_p(t), \quad (6)$$

where  $\mathbf{P}_p(t)$  is the real-time polarization generated by the action of the pump pulse alone, while  $\mathbf{P}_{pp}(t)$  is the real-time polarization generated by the action of both the pump and the probe laser pulse. No dephasing mechanism is included in the simulation in order to preserve the coherent excitonic state generated by the pump laser pulse. While decoherence is expected to happen in experiments, it is far from trivial to formulate a proper decoherence term in Eq. (3). On the contrary, it was shown that dephasing the one-body density matrix, i.e., sending to zero the off-diagonal elements, leads to a noncoherent state, which involves nonbound electron-hole pairs, thus destroying not only coherence but also the excitonic state [20,21]. Instead, a finite broadening parameter  $\eta$  is added later, when performing the Fourier transform of the polarization,

$$\Delta \mathbf{P}(\omega, t_p) = \int_{t_p}^{+\infty} dt \Delta \mathbf{P}(t) e^{i\omega t - \eta(t-t_p)}, \quad (7)$$

where  $t_p$  is the starting time of the probe field. Finally, the nonequilibrium response function is obtained [57,58] dividing by the probe pulse:  $\chi_{\mu\mu}(\omega, t_p) = \Delta \mathbf{P}(\omega, t_p) / \mathbf{E}_p(\omega)$ . The  $\eta$  parameter defines the broadening of the peaks in the response function. The approach can be used to model transient-absorption experiments both in the low-energy range (typically THz of infrared) where exciton-to-exciton transitions are expected, and in the resonant energy range, where shifts and changes to the equilibrium absorption peaks are expected. In the present manuscript, we focus on the low-energy range. Since we have the static HSEX self-energy and we do not include any additional decoherence (or scattering term), the system will remain in the state created by the pump pulse, and the spectra will be independent from  $t_p$ . One of the scopes of the present manuscript is to show that exciton-exciton transition can be captured within TD-HSEX.

## B. Nonequilibrium response function

To analyze the results from the real-time propagation scheme, it is useful to formulate a simplified approach in terms of the excitonic basis set. We start from the general expression for a ‘‘A operator’’-‘‘B operator’’ linear response function [59],

$$\chi_{AB}(\omega) = \frac{2}{V} \sum_{J \neq I} \frac{A_{IJ} B_{JI}}{(E_J - E_I) - \omega - i\eta}. \quad (8)$$

Here the  $I, J$  indexes represent the initial,  $|I\rangle$ , and final,  $|J\rangle$ , many-body states with energies  $E_I$  and  $E_J$ , and  $A_{IJ}$  and  $B_{IJ}$  are the matrix elements of some operator. The dipole-dipole response function is obtained for  $A = \mu^\alpha$ ,  $B = \mu^\beta$ , with the  $\alpha$ th and  $\beta$ th Cartesian component of the matrix element of the many-body dipole operator  $\boldsymbol{\mu}_{IJ} = \langle I | \hat{\boldsymbol{\mu}} | J \rangle$ . The current-current response function instead is obtained for  $A = j^\alpha$ ,  $B = j^\beta$ , with the  $\alpha$ th and  $\beta$ th Cartesian component of the matrix element of the many-body velocity operator  $\mathbf{j}_{IJ} = \langle I | \hat{\mathbf{j}} | J \rangle$ . Both  $\chi_{\mu_\alpha \mu_\beta}$  and  $\chi_{j_\alpha j_\beta}$  can be used to define the optical absorption of a material.  $\epsilon(\omega) = 1 - 4\pi \chi_{\mu_\alpha \mu_\beta}(\omega)$  in the length gauge, or  $\epsilon(\omega) = 1 - 4\pi \chi_{j_\alpha j_\beta}(\omega)/\omega^2$  in the velocity gauge. In the latter case, we explicitly remove the divergent  $1/\omega^2$  and  $1/\omega$  terms by expanding  $\chi_{j_\alpha j_\beta}(\omega)/\omega^2$  and imposing sum rules [60].

At equilibrium the initial state  $|I\rangle = |g\rangle$  is the ground state of the system with  $E_I = E_0$ , and the final state is an exciton state  $|J\rangle = |\lambda \mathbf{q}\rangle$  with  $E_J = E_0 + \omega_\lambda(\mathbf{q})$ . Here  $\mathbf{q}$  is the excitonic momentum index. Assuming that the ground state has zero momentum (i.e., no charge density wave or spin density wave ground state), only zero momentum excitons need to be considered. In this case, the expression of the response function reduces to

$$\chi_{AB}^{\text{eq}}(\omega) = \frac{2}{V} \sum_{\lambda} \frac{A_{0\lambda}(\mathbf{0})B_{\lambda 0}(\mathbf{0})}{\omega_\lambda(\mathbf{0}) - \omega - i\eta}. \quad (9)$$

Within the Tamm-Dancoff approximation (TDA), the exciton states can be expressed as a linear combination of valence-conduction pairs, that is,

$$|\lambda \mathbf{q}\rangle = \sum_{c\mathbf{k}} A_{c\mathbf{k}}^{\lambda \mathbf{q}} |c\mathbf{k} - \mathbf{q}\rangle \otimes |v\mathbf{k}\rangle. \quad (10)$$

Here the  $c$  and  $v$  indexes run over conduction and valence states, respectively, while  $\mathbf{k}$  is the electronic momentum index. The response function obtained by inserting Eq. (10) into Eq. (9) is identical to the one obtained via a formal solution of the many-body response function via many-body perturbation theory (MBPT) within the TDA. It can be shown that the dipole matrix elements  $\boldsymbol{\mu}_{0\lambda}(\mathbf{q}) = \langle \lambda \mathbf{q} | \hat{\boldsymbol{\mu}} | g \rangle$  reduce to a linear combination of single-particle terms (see Appendix A),

$$\boldsymbol{\mu}_{0\lambda}(\mathbf{q}) = e \delta(\mathbf{q}) \sum_{c\mathbf{k}} A_{c\mathbf{k}}^{\lambda 0} \langle c\mathbf{k} | \hat{\mathbf{r}} | v\mathbf{k} \rangle, \quad (11)$$

with  $e$  the electronic charge and  $\hat{\mathbf{r}}$  the one-body position operator. The assumption that the ground state has zero momentum reflects in the  $\delta(\mathbf{q})$  function [61]. The corresponding expression for the matrix elements of the velocity operator  $\mathbf{j}_{0\lambda}(\mathbf{q}) = \langle \lambda \mathbf{q} | \hat{\mathbf{j}} | g \rangle$  can be defined by dividing and multiplying by the transition energies [60]. Neglecting this ratio provides an approximated expression:

$$\mathbf{j}_{0\lambda}(\mathbf{q}) = e \delta(\mathbf{q}) \sum_{c\mathbf{k}} A_{c\mathbf{k}}^{\lambda 0} \frac{\langle c\mathbf{k} | \hat{\mathbf{v}} | v\mathbf{k} \rangle}{\Delta\epsilon_{c\mathbf{k}}} E_\lambda(\mathbf{0}) \quad (12)$$

$$\approx e \delta(\mathbf{q}) \sum_{c\mathbf{k}} A_{c\mathbf{k}}^{\lambda 0} \langle c\mathbf{k} | \hat{\mathbf{v}} | v\mathbf{k} \rangle, \quad (13)$$

where  $\Delta\epsilon_{c\mathbf{k}} = \epsilon_{c\mathbf{k}} - \epsilon_{v\mathbf{k}}$ . The error induced amounts to a renormalization of the peak intensity [60] without significant changes in the equilibrium absorption. Equation (12) cannot be used when  $\Delta\epsilon_{nm\mathbf{k}} < \epsilon_{\text{thresh}}$  since the ratio  $\langle c\mathbf{k} | \hat{\mathbf{v}} | v\mathbf{k} \rangle / \Delta\epsilon_{c\mathbf{k}}$

becomes numerically unstable. This is also related to the fact that intraband matrix elements  $\langle n\mathbf{k} | \hat{\mathbf{v}} | n\mathbf{k} \rangle = \langle n\mathbf{k} | \hat{\mathbf{v}} | n\mathbf{k} \rangle / \Delta\epsilon_{nm\mathbf{k}}$  are ill-defined since  $\Delta\epsilon_{nm\mathbf{k}} = 0$ . In our code,  $\epsilon_{\text{thresh}} = 10^{-5}$  eV. While at equilibrium this never happens in systems with a gap, transitions with  $\Delta\epsilon_{nm\mathbf{k}} < \epsilon_{\text{thresh}}$  will be involved in the TR-abs spectrum [see the later discussion around Eq. (17)].

In the nonequilibrium regime, we assume that an excitonic state has been created by the pump laser pulse,  $|I\rangle = |\lambda_i \mathbf{q}\rangle$  with  $E_I = E_0 + \omega_{\lambda_i}(\mathbf{q})$ , where the superscript “ $i$ ” is used to highlight that this is the initial excitonic state. The nonequilibrium dipole-dipole response function in the energy range of interexciton transitions takes the form (see also Appendix B)

$$\chi_{\mu_\alpha \mu_\beta}^{\lambda_i \mathbf{q}}(\omega) = \frac{2}{V} \sum_{\lambda} \frac{\mu_{\lambda_i \lambda}^\alpha(\mathbf{q}) \mu_{\lambda \lambda_i}^\beta(\mathbf{q})}{\omega_\lambda(\mathbf{q}) - \omega_{\lambda_i}(\mathbf{q}) - \omega - i\eta}. \quad (14)$$

Equation (14) holds at low excitonic densities because we are assuming that the equilibrium excitonic energies and wave functions can be used, and because no final-state population effects are considered [62]. The intensity of the transient absorption signal is weighted by the exciton density injected by the pump pulse.

We observe that for optically injected excitons, the condition  $\mathbf{q} = \mathbf{0}$  holds, however dissipation and relaxation mechanisms could scatter the initial state into finite momentum excitonic states leading to a population  $N_{\lambda_i}(\mathbf{q})$ , and the overall transition signal can be expressed as

$$\chi_{\mu_\alpha \mu_\beta}(\omega) = \sum_{\lambda_i \mathbf{q}} N_{\lambda_i}(\mathbf{q}) \chi_{\mu_\alpha \mu_\beta}^{\lambda_i \mathbf{q}}(\omega). \quad (15)$$

This is why, in general, even in the presence of an optical pump and an optical probe, finite momentum excitons need to be considered to model interexciton transitions. The above expression assumes that the noncoherent populations do not give rise to interference patterns in the transient absorption signal. In the present manuscript, we do not account for relaxation and dissipation mechanisms, and we will focus on the situation in which  $N_{\lambda_i}(\mathbf{q}) = N^{\text{exc}} \delta_{\lambda_i, \lambda_0} \delta(\mathbf{q})$ .

### C. Selection rules

The crucial step is then to identify the dipole-allowed  $\lambda \rightarrow \lambda'$  transitions. Starting from the hydrogen model, and dividing exciton-exciton transitions into intra- and interexciton transition [33], selection rules for the intraexciton transitions can then be established starting from the quantum numbers of the hydrogen model used to describe the exciton. However, this approach neglects the symmetries of the crystal in the excitonic envelope, and it is a good approximation only for delocalized Wannier excitons. For more localized Frenkel excitons, a fully *ab initio* approach, and/or an approach that accounts for the symmetries of the lattice, offers a better description.

#### 1. *Ab initio* dipole matrix elements

In the *ab initio* formalism, selection rules can be computed explicitly by defining the expression for the dipole matrix elements  $\boldsymbol{\mu}_{\lambda \lambda'}(\mathbf{q}) = \langle \lambda \mathbf{q} | \hat{\boldsymbol{\mu}} | \lambda' \mathbf{q} \rangle$  (see the derivation in



Appendix A 2):

$$\begin{aligned} \boldsymbol{\mu}_{\lambda_i\lambda}(\mathbf{q}) = & \sum_{v,cc',\mathbf{k}} (A_{cv\mathbf{k}}^{\lambda\mathbf{q}})^* A_{c'v\mathbf{k}}^{\lambda_i\mathbf{q}} \mathbf{r}_{cc'\mathbf{k}} \\ & - \sum_{c,vv',\mathbf{k}} (A_{cv\mathbf{k}}^{\lambda\mathbf{q}})^* A_{c'v'\mathbf{k}}^{\lambda_i\mathbf{q}} \mathbf{r}_{v'v\mathbf{k}-\mathbf{q}} \\ & + \sum_{v,c,\mathbf{k}} (A_{cv\mathbf{k}}^{\lambda\mathbf{q}})^* A_{c'v\mathbf{k}}^{\lambda_i\mathbf{q}} \sum_{n \in occ} \mathbf{r}_{nm\mathbf{k}}. \end{aligned} \quad (16)$$

The dipole matrix elements depend both on the excitonic coefficients  $A_{cv\mathbf{k}}^{\lambda\mathbf{q}}$  and on the interband dipoles  $r_{nm\mathbf{k}}$  over all the  $\mathbf{k}$ -points of the BZ. Equation (16) is a generalization of the simplified analysis of Ref. [34], which holds for delocalized Wannier excitons, in which the dipole matrix element  $\boldsymbol{\mu}_{\lambda_i\lambda}(\mathbf{q})$  depends only on the excitonic wave functions and their quantum numbers in the hydrogenic model.

The first two addends of (16) have a very simple interpretation in terms of transitions from state  $\lambda_i$  to state  $\lambda$  mediated by the electronic dipole. Their expression is very similar to that of the exciton-phonon matrix elements [18], although it involves only one momentum, since the initial and final exciton must have the same momentum. However, an issue appears since Eq. (16) involves the intraband dipoles  $\mathbf{r}_{nm\mathbf{k}}$ , which are ill-defined in periodic boundary conditions. This points to the fact that we are looking to a nonlinear response, as discussed in the Introduction. Moving to the velocity gauge and to the current-current response function solves this issue, since intraband velocity dipoles are well-defined,

$$\begin{aligned} \mathbf{j}_{\lambda_i\lambda}(\mathbf{q}) \approx & \sum_{v,cc',\mathbf{k}} (A_{cv\mathbf{k}}^{\lambda\mathbf{q}})^* A_{c'v\mathbf{k}}^{\lambda_i\mathbf{q}} \mathbf{v}_{cc'\mathbf{k}-\mathbf{q}} \\ & - \sum_{c,vv',\mathbf{k}} (A_{cv\mathbf{k}}^{\lambda\mathbf{q}})^* A_{c'v'\mathbf{k}}^{\lambda_i\mathbf{q}} \mathbf{v}_{v'v\mathbf{k}} \\ & + \sum_{v,c,\mathbf{k}} (A_{cv\mathbf{k}}^{\lambda\mathbf{q}})^* A_{c'v\mathbf{k}}^{\lambda_i\mathbf{q}} \sum_{n \in occ} \mathbf{v}_{nm\mathbf{k}}. \end{aligned} \quad (17)$$

The velocity gauge introduces an overall error in the intensity of the dipoles [similarly to the equilibrium case; see the previous discussion related to Eq. (12)] [60]. At variance with the equilibrium case, however, we cannot divide by the transition energies  $\Delta\epsilon_{nm\mathbf{k}}$  and later multiply by the excitonic energies, since this operation is numerically unstable for  $\Delta\epsilon_{nm\mathbf{k}} < \epsilon_{\text{thresh}}$  and ill-defined for the case  $\Delta\epsilon_{nm\mathbf{k}} = 0$ . Thus, we use Eq. (17) when computing the spectra in the velocity gauge, which, in short, introduces an overall error in the intensities, but accounts for the role of intraband transitions.

Finally, we underline that in the presence of degenerate excitonic states, it is crucial to identify a specific state in the degenerate subspace to describe the exciton generated by the pump pulse. The polarization of the selected exciton must be parallel to the field polarization projected into the polarization space spanned by the degenerate excitons. This allows us to capture the dependence of the transient absorption spectrum on the relative orientation of the pump and the probe pulse polarization. In Appendix C we show how this dependence can be taken into account.

## 2. Symmetry considerations

In support of the real-time calculations and the nonequilibrium response functions, we provide a symmetry analysis of the different spectra presented in this work. In particular, we analyze the matrix elements

$$\boldsymbol{\mu}_{IF} = \langle F | \hat{\boldsymbol{\mu}} | I \rangle \quad (18)$$

that enter in Eq. (14) using group theory [63] in such way as to determine which matrix elements are zero by symmetry and which are not. To do this, we assign each of the three elements in Eq. (18),  $\langle F |$ ,  $\hat{\boldsymbol{\mu}}$ , and  $| I \rangle$ , the irreducible representation (irreps) to which it belongs, with respect to the symmetry group of the crystal. Let us call them  $O_F$ ,  $O_\mu$ , and  $O_I$ . Then the integral is different from zero *if and only if* the identity element belongs to the product of the three symmetry operations [63]. This result can be achieved using the product table of the symmetry point group, and furthermore also polarization effects can be taken into account by considering the ‘‘partner’’ (here we use the same nomenclature of Ref. [63]) of each irrep associated with a specific polarization. This analysis is performed in detail for the point groups of the two materials considered in Appendix B of the present manuscript.

## III. RESULTS

In this section, we will compute the Tr-Abs properties of LiF and hBN using the two approaches discussed in the previous section. We will label ‘‘TD-HSEX’’ results those obtained from the real-time propagation scheme, and ‘‘Exc. Fermi’’ results based on the Fermi golden rule in the excitonic space. In particular, ‘‘Exc. Fermi (length)’’ if the TR-Abs is constructed via Eq. (16) and ‘‘Exc. Fermi (velocity)’’ via Eq. (17). It is worth mentioning that, while the TD-HSEX scheme describes the exciton-exciton transition starting from a coherent excitonic state, the Exc. Fermi approach describes the exciton-exciton transition starting from a noncoherent excitonic population. However, as already shown for the case of ARPES, the two give rise to the same signal, provided that the average population of the coherent state is equal to the population of the noncoherent state. Eventual differences due to the coherent polarization associated with the excitonic state, such as Franz-Keldysh oscillations in the TR-Abs spectra, could be observed only in specific conditions [57]. This is beyond the scope of the present manuscript.

### A. Results on LiF

LiF is a wide-gap insulator, with an electronic band gap of  $\approx 14.5$  eV (experimental data give a gap in the range 14.1–14.5 eV, while *GW* simulation on top of LDA gives a value close to 14.4 eV [45]). The absorption spectrum is dominated by an intense excitonic peak ( $E_1$ ) at  $\approx 12.5$  eV [see the panel (a) of Fig. 1].  $E_1$  has often been described as a charge transfer (CT) exciton, involving transfer of an electron from the alkaline atom (Li)  $p$  to a halogen atom (F)  $s$  level [49]. This description emerges from the fact that LiF is an ionic crystal, in which the lone Li( $2s$ ) electron of the isolated Li atom is transferred to the empty F( $2p$ ) level of the F atom. Accordingly, the valence-band structure is mainly composed

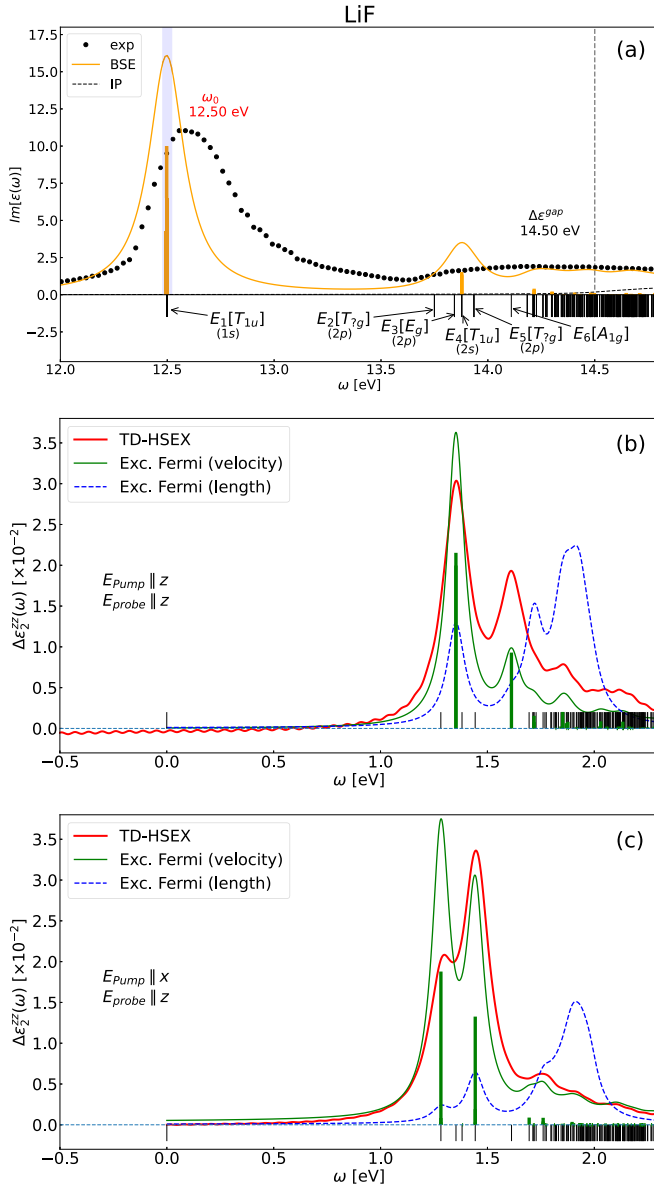


FIG. 1. (a) Absorption of LiF. All poles  $\omega_\lambda$  are represented as vertical black lines. Orange vertical bars are proportional to  $|\mu_{0\lambda}(\mathbf{0})|^2$ . (b),(c) Transient absorption of LiF after pumping the system with a pump resonant with the first excitonic pole  $\omega_1$ . All possible transitions  $\Delta\omega = \omega_i - \omega_1$  are represented with vertical black lines. Green vertical bars are proportional to  $|\mathbf{j}_{\lambda\lambda_i}(\mathbf{0})|^2/\omega^2$ . (b) Configuration with probe parallel to the pump. (c) Configuration with probe perpendicular to the pump.

by the F(2p) orbitals, while the lowest conduction band is the Li(2s) states.  $E_1$  has been studied in different works and, while initially proposed as intermediate between Frenkel and Wannier, it has more recently been identified as a strongly bound Frenkel exciton [49]. Due to its large binding energy of  $\approx 2$  eV, it has often been used to validate theoretical development. For example, its wave function [4,5] and dispersion [52] were analyzed in detail. Other excitons, involving a semicore hole in the XUV energy range, have been investigated in the literature by means of *ab initio* simulations [50], reporting even larger binding energies.

Instead, less attention has been paid to the excitons, either dark or bright, which lie in the energy window between  $E_1$  and the electronic gap, and which characterize the excitonic series of LiF. In the present work, we investigate these excitons which, after the action of a laser pulse tuned resonant with  $E_1$ , dominate the transient absorption spectrum of LiF in the energy range from 0 to 2 eV. We label them  $E_2, E_3, E_4, \dots$ .

We employ the standard GW+BSE scheme on top of LDA. Ground-state LDA calculation are performed with norm-conserving pseudopotentials, an energy cutoff of 80 Ry for the wave functions, and a  $6 \times 6 \times 6$   $k$ -points grid. RPA screening is computed with a cutoff of 8 Ry for the response function  $\chi_{GG'}(\mathbf{q}, \omega)$  and using 50 bands in the internal sum over the conduction states. Finally, the BSE calculation is performed with a scissor of 6.05 eV, bands from 2 to 5,  $k$ -points grid  $24 \times 24 \times 24$ , an energy cutoff 8 Ry for the screened  $e-h$  interaction  $W_{GG'}$ , and 32 Ry for the  $e-h$  exchange interaction  $v_G$ . The same parameters are then used for the real-time propagation within the TD-HSEX simulations, with the bands 2 to 5 entering the bands indexes in Eq. (3) and in Eqs. (E2) and (E3),  $k$ -points grid  $24 \times 24 \times 24$ , 8 Ry for  $W_{GG'}$ , and 32 Ry for  $v_G$ . Moreover, a time step of  $10^{-2}$  femtoseconds (fs) is used to time integrate Eq. (3) with the Crank-Nicolson integrator for a total time of 100 fs, which is later used to integrate Eq. (7).

In Fig. 1, absorption and transient absorption of LiF are shown. The solution of the excitonic matrix shows several bound poles, many of which are dark. The first six poles are well-separated from the others. In addition to the well-characterized lowest energy bright exciton  $E_1$ , also  $E_4$  is bright, while the other four are dark; see panel (a) of Fig. 1. The position of the bright exciton  $E_4$ , around 13.9 eV, seems to be confirmed by the shape of the experimental absorption, which bounces back at around 13.7 eV, although with a very broad signal. All bright poles are threefold-degenerate, due to the symmetries of the crystal, while dark poles can have different degeneracy. The poles from  $E_2$  to  $E_5$  are located in the energy range between 13.78 and 13.94 eV.  $E_2$  and  $E_5$  are also threefold-degenerate, while  $E_3$  is twofold-degenerate. Finally,  $E_6$  is shifted from the previous group at 14.1 eV and it is nondegenerate.

Turning our attention from equilibrium absorption to transient absorption in the interexciton transitions regime, first of all we observe that the TD-HSEX scheme gives poles exactly at the energy differences  $E_i - E_1$ , with  $i$  running over the other excitons. Such a result can be obtained only using the Berry phase expression for the polarization, Eq. (5). Using instead TD-HSEX with Eq. (4) gives a zero spectrum in this energy range, regardless of the  $\epsilon_{\text{thresh}}$  value. Moreover, it is remarkable that, after pumping the system in resonance with the lowest-energy excitons, the four dark poles mentioned above can be detected by considering two different configurations: probe parallel to the pump pulse [Fig. 1(b)] and probe perpendicular to the pump pulse [Fig. 1(c)]. This result shows that transient absorption is a very powerful technique to explore dark excitonic poles. In both configurations, we show the transient absorption spectra computed by a full real-time propagation scheme at low pump intensity (red continuous line) and the spectra obtained within the “excitonic Fermi

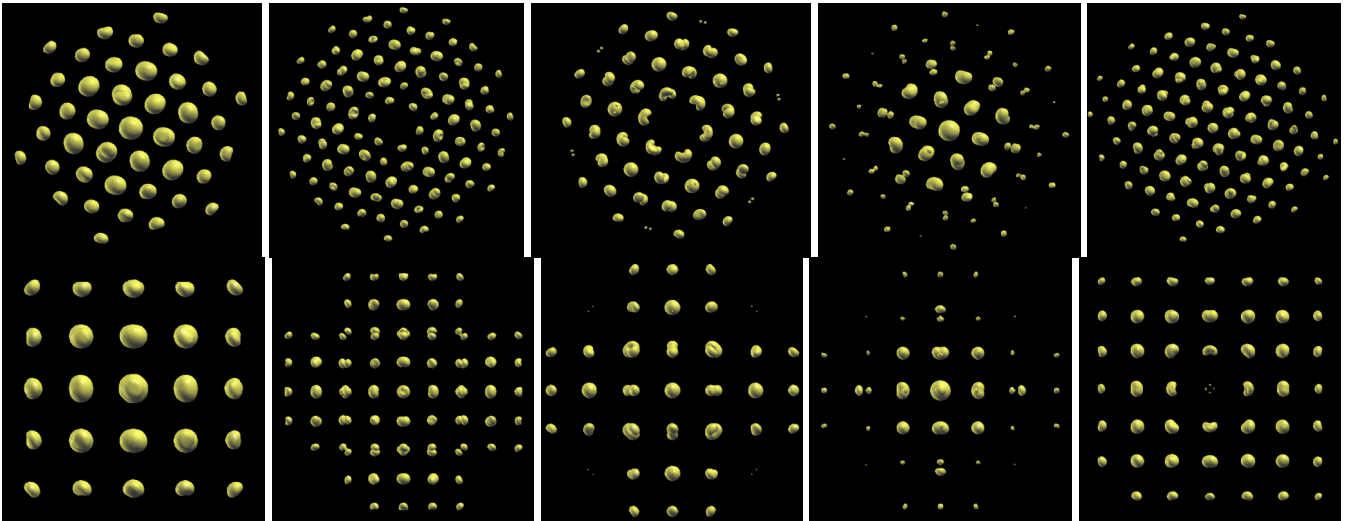


FIG. 2. Exciton density for the first five excitons of LiF at fixed hole position. Upper row, view along the 111 direction. Lower row, view along the 100 direction. The hole position is put near a F atom at the center of the picture. The density is averaged over degenerate excitons. All excitons are threefold-degenerate, with the exception of the third, which is two fold-degenerate.

golden rule,” either in the length gauge (blue dashed line) or in the velocity gauge (green continuous line). As discussed in Sec. II, both gauges have some issues and are not able to precisely reproduce the results of the full real-time propagation. Indeed, both blue and green lines correctly foresee which interexciton transitions are expected to be bright, but somehow they miss the correct relative intensity. The problem is much more severe in the length gauge, which strongly underestimates the intensity of the low-energy peaks and overestimates the intensity of the higher-energy ones. The velocity gauge tends to do the opposite, but the agreement with the full real-time propagation is much better and, overall, the velocity gauge approach can be used to obtain a good description of the spectra.

We want now to understand why some transitions are bright, depending on the relative orientation of the pump and the probe pulse. A first qualitative explanation can be sought by pursuing the common approach used in literature, based on the simple hydrogenic model for the excitonic states. To this end we perform a direct inspection of the excitonic wave function and we try to label the excitonic envelope as *s* or *p* states. The overall wave-function symmetry will be the product of the symmetry of the envelope,  $A_{cv\mathbf{k}}^\lambda$ , and the symmetries of the underlying Bloch states,  $\psi_{c\mathbf{k}}^*(\mathbf{r}_e)$  and  $\psi_{v\mathbf{k}}(\mathbf{r}_h)$ . To this end, we first notice that for LiF the symmetry group is  $O_h$ , which has 48 symmetry operations and 10 irreducible representation (for the irreps, see Appendix B). Transitions belonging to the  $T_{1u}$  irrep are bright at equilibrium. The  $F(2p)$  orbitals of the conduction band are associated with the  $T_{1u}$  irrep, while the  $Li(2s)$  are associated with the  $A_{1g}$  irrep [63]. Since  $T_{1u} \times A_{1g} = T_{1u}$ ,  $Li(2s) \rightarrow F(2p)$  transitions are dipole-allowed. The first six poles  $E_1 \cdots E_6$  all involve these orbitals. Accordingly, we can label the exciton-exciton transition involving  $E_1 \cdots E_6$  as *intraexciton* transitions, which are controlled by the envelope of the excitonic wave function.

We thus turn our attention to the description of the envelope. In Fig. 2, the square modulus of the excitonic wave

functions

$$\Psi_\lambda(\mathbf{r}_e, \mathbf{r}_h) = \sum_{cv\mathbf{k}} A_{cv\mathbf{k}}^\lambda \psi_{c\mathbf{k}}^*(\mathbf{r}_e) \psi_{v\mathbf{k}}(\mathbf{r}_h) \quad (19)$$

is plotted as a function of the electronic coordinate and by fixing the hole coordinate near one F atom. In all the considered excitonic states, the wave functions display non-negligible electronic density only on the F atoms. Even though this fact was already observed for the lowest energy exciton [4], and also studied with some details [64], it goes against the intuition of the LiF excitons described in terms of CT excitons, due to the nature of the valence- and conduction-band structure, which remain used in many model calculations [49,51]. In terms of the hydrogenic model for the exciton, since  $Li(2s) \rightarrow F(2p)$  already fulfill the selection rules, bright excitons at equilibrium are expected to have  $l = 0$ . Instead in the nonequilibrium spectrum, it is only the envelope that determines if exciton-exciton transitions are allowed. Dipole-allowed transitions should respect  $\Delta l = \pm 1$  and  $\Delta m_l = 0, \pm 1$  [33].

Inspecting the plot of the excitonic wave function, the two bright excitons  $E_1$  and  $E_4$  are the only ones where the electronic density sits in the same atom as the hole. The lowest energy  $E_1$  exciton in the literature has been identified as a  $1s$  exciton [4].  $E_4$  can be identified as the  $2s$  exciton. For the other dark excitons, the electronic charge is on the nearest-neighbor F atoms, as can be seen either from the 111 ( $E_2$  and  $E_3$ ) or the 110 ( $E_5$  exciton) view, since in all cases there is a negligible electron density in the center of the image. Accordingly, we can tentatively label as *p*-like these dark states. This would explain why these excitons can be seen in the transient spectrum starting from the  $1s$  exciton. However, within this scheme, we are not able to explain why some are bright when the pump and probe are parallel, while others are bright when the pump and probe are perpendicular.

A satisfactory analysis of the selection rules governing the transitions among exciton states can be performed only by

considering the space group representation of crystal lattice *also* for the excitonic envelope. Let us start with the bright excitons. An  $s$  envelope in  $O_h$  corresponds to  $A_{1g}$  symmetry without any energy lifting [63], and overall the symmetry of the excitonic wave function for  $E_1$  and  $E_4$  is

$$[s\text{-envelope}] \times [F(2s) \rightarrow L(2p)] = A_{1g} \times T_{1u} = T_{1u},$$

which explains why they are bright and threefold-degenerate as already observed. A  $2p$  envelope in  $O(h)$  is associated with  $T_{1u}$  symmetry, again without any energy lifting. The overall symmetry of the underlying excitons is then

$$\begin{aligned} [2p\text{-envelope}] \times [F(2s) \rightarrow L(2p)] &= T_{1u} \times T_{1u} \\ &= A_{1g} + E_g + T_{1g} + T_{2g}. \end{aligned}$$

We now need to assign to each exciton the correct representation. We can use the exciton multiplicity, and, again, the knowledge of how a given irrep in  $O_h$  can be related to a given angular momentum. The four resulting irreps can all originate by the lifting of spherical states with even angular momentum. However,  $T_{2g}$  and  $E_g$  can originate from states with  $l \geq 2$ , while  $T_{1g}$  and  $A_g$  from states with  $l \geq 3$  [63]. Thus we expect that the two lowest-energy excitons should come from  $T_{2g}$  and  $E_g$  (i.e., we assume lower angular momentum implies lower energy), and looking at the exciton multiplicity we can assign  $E_2[T_{2g}]$  and  $E_3[E_g]$ . The ordering is in agreement with the well-known energy splitting of  $d$  orbitals in  $O_h$  symmetry, i.e.,  $E_2[T_{2g}] < E_3[E_g]$ . Since  $E_6$  is nondegenerate,  $E_6[A_{1g}]$ , and we tentatively assign  $E_5[T_{1g}]$ .

We can now use this analysis to predict which exciton-exciton transitions are allowed. First of all we notice that, out of the 10 irreps operations, only the states belonging to the irreps  $A_{1g}$ ,  $E_g$ ,  $T_{1g}$ , and  $T_{2g}$  are bright (see again Appendix B). These are exactly the four irreps that originate from the  $2p$  excitons, and it means that all four dark excitons are expected to be visible in the Tr-Abs spectrum. Moreover, the relative polarization of the pump and probe pulses can alternatively select different excitons. More specifically, the allowed bright representations need to transform as the corresponding quadratic function of the coordinates consistently with the polarization choice of the pump and probe pulses. So, when the pump and probe are both parallel to the  $x$  axis, we see that  $A_{1g}$  and  $E_g$  are expected to be detected. Instead, for perpendicular pump and probe,  $T_{2g}$  and  $T_{1g}$  are seen. Indeed, we see from the middle panel of Fig. 1 that  $E_3[E_g]$  and  $E_6[A_{1g}]$  are bright, while  $E_2[T_{2g}]$  and  $E_5[T_{1g}]$  are bright in the lower panel. This confirms our previous analysis. Finally, we observe that  $T_{1u} \rightarrow T_{1u}$  transitions are dipole-forbidden. Starting from the excited  $1s$  state injected by the pump laser pulse (i.e., the state in the  $T_{1u}$  multiplet with polarization parallel to the pump pulse polarization, which we call  $T_{1u}^x$  partner [63]), the transitions towards the other two degenerate states ( $T_{1u}^y$  and  $T_{1u}^z$ ) of the multiplet are dipole-forbidden.

### 1. Strong pumping regime

We conclude the discussion on LiF by showing how the shape of the TrAbs spectrum changes as a function of the pump fluence. Results are shown in Fig. 3. The exciton Fermi golden rule approach is not able to reproduce the evolution of the spectrum in this regime, and only the real-time

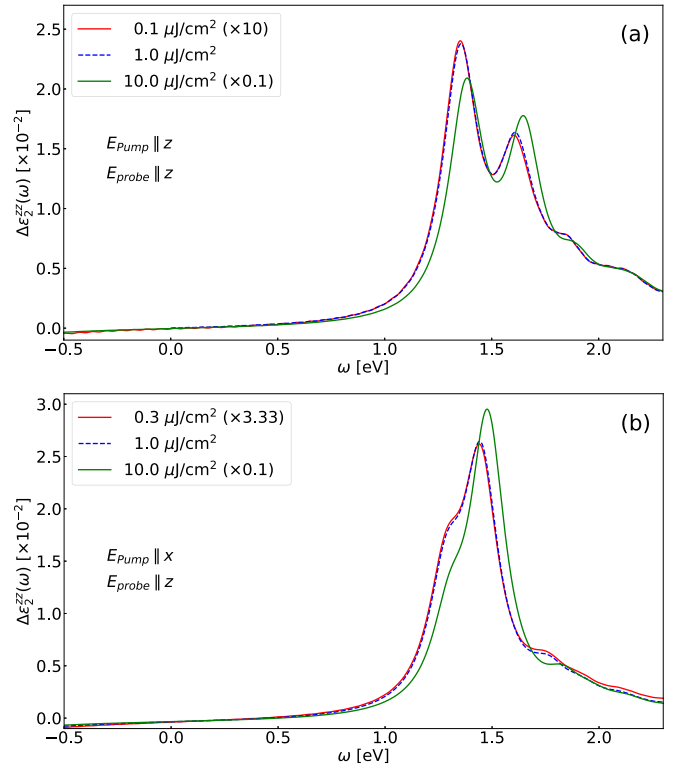


FIG. 3. Transient absorption defined as in Fig. 1 as a function of the pump fluence. The reported values for the laser fluence refer to the field inside the sample, i.e., they should be corrected taking into account the fraction of the laser pulse which is reflected when compared with nominal experimental fluences. Compared to Fig. 1, a larger broadening parameter is used here.

propagation scheme can be used. Increasing the pump fluence, and accordingly the initial exciton density, the energy required for the interexciton transition is blueshifted for the first four dark excitons explored in the manuscript. The intensity of the transition  $E_1 \rightarrow E_3$  is reduced, while that for the transition  $E_1 \rightarrow E_6$  is enhanced (parallel configuration); the intensity for the transition  $E_1 \rightarrow E_2$  is reduced, while that of the transition  $E_1 \rightarrow E_4$  is enhanced (perpendicular configuration). Inspecting the numerical simulations (and also from the experimental and theoretical literature on TrAbs in the resonant probe regime) we know that the energy position of the  $E_1$  peak is blueshifted due to many-body effects [65,66]. For the considered fluences, the injected exciton density is roughly linear with the pump fluence. With a fluence of  $1 \mu\text{J}/\text{cm}^2$  we obtain an exciton density of  $1.7 \times 10^{-4} \text{ exc.}/\Omega$ , with  $\Omega$  the unit-cell volume. This corresponds to a total density of  $\approx 10^{19} \text{ exc.}/\text{cm}^3$ . Given the very large binding energy and the very small exciton radius of  $E_1$  in LiF ( $r_{\text{exc}} \approx 5 \text{ \AA}$ ), we expect the critical exciton Mott transition density ( $n_{\text{Mott}} \sim r_{\text{exc}}^{-3}$ ) to be well above  $10^{20} \text{ exc.}/\text{cm}^3$  [67]. The overall blueshift of the  $E_1 \rightarrow E_l$  transitions implies that the higher-energy peaks are shifted even more. Moreover, the relative changes in the intensity of the peaks imply not only that the excitons shift, but also that there are changes in the excitonic wave functions that renormalize the expectation value of the intraexciton dipole matrix elements.



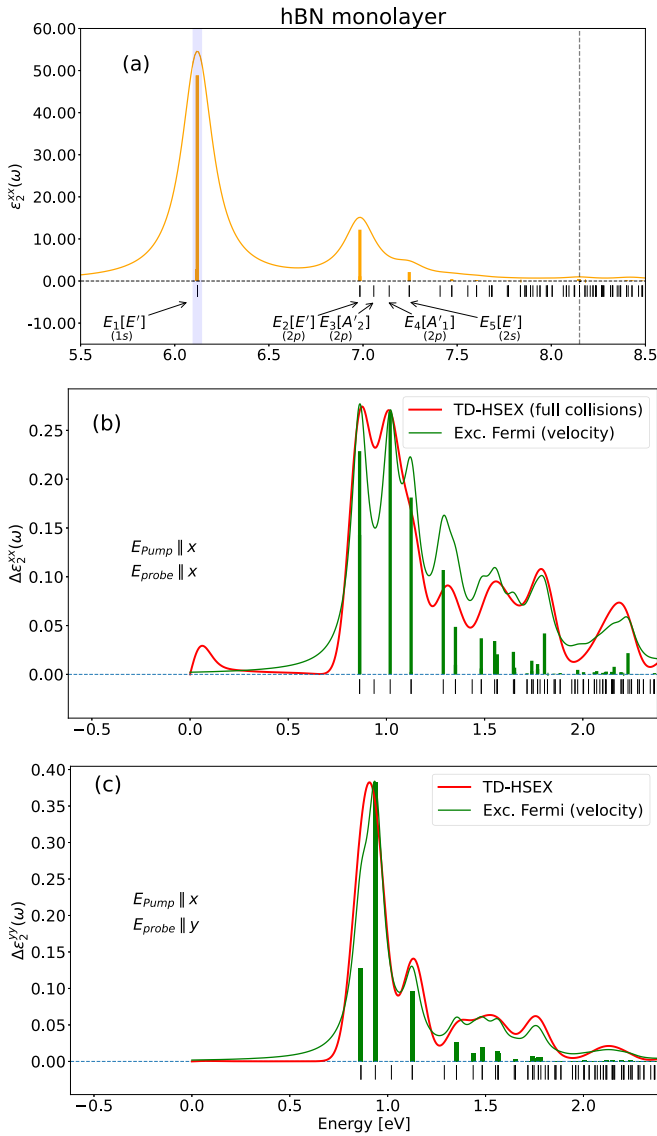


FIG. 4. Equilibrium absorption (a) of a hBN monolayer [69] and pump and probe spectra (b),(c) for the monolayer hBN. In the top panel both the pump and probe are in the  $x$  direction, while in the bottom panel the pump is along  $x$  while the probe is along  $y$ . We report in green the excitonic levels at equilibrium and their symmetry for the first four [7].

## B. Monolayer hexagonal BN

The structure of electron-hole excitations in monolayer hBN (m-hBN) is well known from theory and experiments [7]. In particular, recent measurements probed for the first time the lowest excitonic state of single-layer hBN deposited on a substrate [68]. The electronic excitation of m-hBN can be classified according to the representations of the  $D_{3h}$  point group (see also Appendix B 2). In panel (a) of Fig. 4 we report the computed optical absorption [69] of monolayer hBN with in-plane polarization. The exciton classification for the first five excitonic peaks— $E_1[E']$ ,  $E_2[E']$ ,  $E_3[A'_2]$ ,  $E_4[A'_1]$ , and  $E_5[E']$ —is taken from Ref. [7]. Among the different group representations, only the two-dimensional irrep  $E'$  is optically active for in-plane polarization [63], while excitons belonging to the  $A'_2$  irrep are bright for out-of-plane polarization (i.e.,

along the  $z$  direction). In the present manuscript, we focus on the in-plane polarization. In Ref. [7], these excitons are also mapped into the hydrogen series by comparing *ab initio* and tight-binding simulations. A similar analysis is also performed in Ref. [70]. The lowest exciton  $E_1[E']$  can be identified as the  $1s$  exciton, and it has a very strong oscillator strength. The next three excitons,  $E_2[E']$ ,  $E_3[A'_2]$ , and  $E_4[A'_1]$ , originate from a  $2p$ -like state, and at variance with the LiF case, they are not all dark. Finally, the fifth exciton  $E_5[E']$  originates from a  $2s$  state. The states with  $A'_1$  symmetry have been measured in two-photon absorption experiments [28], while other states are usually inaccessible because of their too high energy.

As in the LiF, here we show how pump and probe spectroscopy can be used as an alternative technique to the one- and two-photon absorption to study excitons in this material. Pump and probe spectroscopy presents a double advantage, first the possibility of studying excitons that are dark in linear optics, and second the possibility of studying high-energy excitons that usually are inaccessible to standard laboratory facilities due to the large band gap of hBN [71]. To simulate pump and probe spectroscopy in a monolayer hBN, we used a supercell with an in-plane lattice parameter of  $a = 2.5 \text{ \AA}$  and a distance between the periodic replica of  $c = 30 \text{ a.u.}$  We constructed the dielectric constant that enters in the BSE and SEX self-energy using 100 bands and 20 Ry cutoff, plus a terminator to speed up convergence on the conduction bands [72]. In the optical spectra and real-time dynamics, we include two valence and two conduction bands, and a scissor of 3.66 eV. The equations of motion in real time were propagated for 165 fs using the same algorithm and parameters of the LiF case. We also restrict ourselves to the case in which the probe polarization is in the plane. In panels (b) and (c) of Fig. 4 we report the pump and probe spectra for the hBN monolayer in two different cases. In panel (b) both the pump and the probe are in the  $x$  direction, while in panel (c) the pump is along  $x$  and the probe along the  $y$  direction. Similarly to the LiF case, we observe that the TD-HSEX scheme gives poles exactly at the energy differences  $E_i - E_1$ , with  $i$  running over the other excitons. In the same panels, we report also the pump and probe spectra calculated using the Fermi golden rule approach discussed in Sec. II B within the velocity gauge. The comparison between the two approaches shows very good agreement, emphasizing that the approximations made in Sec. II B introduce only a marginal error in the final spectra. However, at variance with the case of LiF, we have an instability in the real-time numerical simulations for the case of probe parallel to the pump, which gives a small peak at  $\omega \approx 0$ .

By performing a group theory analysis similar to the LiF case (see Appendix B 2), we find that for the parallel pump and probe only excitons with  $E'$  and  $A'_1$  symmetry can be excited starting from the lowest exciton  $1s$  with  $E'$  symmetry, while for the perpendicular pump and probe field the excitons with  $E'$  and  $A'_2$  symmetry are accessible. This means that bright states are also visible in the transient spectra and in both geometries. This is due to the lower symmetry of the  $D_{3h}$  group, and it has another remarkable consequence. This theoretical prediction is confirmed by our real-time numerical simulations [73]. Let us remark on the

consequences of this, and how much hBN is different from LiF. In the case of LiF, the hydrogen atom selection rules  $\Delta l = \pm 1$  are not able to predict which transition will be activated by fixing the relative polarization of the pump and the probe. However, they are enough to predict that only  $1s \rightarrow 2p$  transitions are dipole-allowed at low energy. In hBN instead,  $\Delta l = \pm 1$  is not fulfilled at all, since the  $1s \rightarrow 2s$  transition, i.e., the  $E_1[E'] \rightarrow E_5[E']$  transition, is now dipole-allowed. Moreover the almost degenerate  $1s \rightarrow 1s$ , i.e.,  $E_1^x[E'] \rightarrow E_1^y[E']$  energy transitions are now also dipole-allowed. This is why a low-energy peak appears in the numerical simulations. The exact energy of this peak will depend on the injected exciton density, which would be responsible for slightly lifting the degeneracy between the two states belonging to  $E'$ . We did not try to converge it numerically and, moreover, we are not yet able to explain why it appears only in the parallel pump probe polarization configuration. Still, it is a remarkable result that such a transition can be seen in the simulation and a fingerprint that at very low energy the probe pulse is in principle able to spatially rotate the polarization induced by the pump pulse in the  $xy$  plane, a mechanism that is not allowed in LiF.

#### IV. CONCLUSIONS

In this article, we studied exciton-exciton transitions in transient absorption experiments by performing accurate *ab initio* real-time simulations, which couples the TD-HSEX scheme with the Berry phase expression for the polarization. To interpret the results obtained via this real-time scheme, we also develop a Fermi golden rule approach based on the assumption that the initial state created by the pump laser pulse can be well described as a quasiequilibrium state with a well-defined excitonic population. In this way, the nonequilibrium response can be analyzed in terms of transitions between different excitons. Starting from the excitonic wave functions computed with the *ab initio* Bethe Salpeter equation, we define the dipole elements between the different excitonic states, and we use them to calculate the nonequilibrium response function. This is also corroborated by a detailed group theory analysis of the excitonic states.

The agreement obtained via the formally more rigorous real-time propagation schemes shows that for laser pulse intensities compatible with many pump and probe experiments, bound excitons such as those in LiF and hBN behave as well-defined quasiparticles. Moreover, it offers a validation of the Fermi golden rule approach, which is numerically much cheaper, and potentially interesting for future applications. While the real-time propagation scheme could be employed to study the effect of increasing exciton density as well as the relaxation and dissipation mechanism, the exciton Fermi golden rule approach provides a cheaper approach, where also the signature of finite momentum excitons into Tr-Abs spectra can be investigated.

Finally, these results show that absorption spectroscopy in the exciton-exciton energy range offers new opportunities to study high-energy excited states not accessible by other spectroscopic techniques. The technique is also a very powerful tool to measure exciton relaxation and exciton dynamics.

#### ACKNOWLEDGMENTS

This publication is based upon work from COST Action TUMIEE CA17126, supported by COST (European Cooperation in Science and Technology). The work was also supported in part by European Union project MaX Materials design at the eXascale H2020-EINFRA-2015-1 (Grant Agreement No. 824143) and by Italian Miur PRIN (Grants No. 20173B72NB and No. 2020JZ5N9M), and the ANR grant Colibri (Project No. ANR-22-CE30-0027). C.A. acknowledges A. Saul and K. Boukari for the management of the computer cluster *Rosa*. D.S. acknowledges useful discussions with Fulvio Paleari.

#### APPENDIX A: DERIVATION OF THE DIPOLE MATRIX ELEMENTS

In this Appendix, we present the derivation of dipole matrix elements between different excitonic states, both in the equilibrium and nonequilibrium cases.

##### 1. Equilibrium case: Ground state to exciton transition

First we derive Eq. (11) in the formalism of second quantization. This is a well-known result, and the derivation is reported here just as a preliminary step toward the derivation of Eq. (16). We introduce the creation operator  $\hat{a}_{nk}^\dagger$  which creates an electron in the state  $|nk\rangle$  acting on the many-body vacuum state  $|0\rangle$ . The GS and the valence-conduction pair are written as

$$|g\rangle = \prod_{v\mathbf{k}}^{\nu} \hat{a}_{v\mathbf{k}}^\dagger |0\rangle, \quad |c\nu\mathbf{k}\rangle = \hat{a}_{c\mathbf{k}}^\dagger \hat{a}_{v\mathbf{k}} |g\rangle. \quad (\text{A1})$$

The (many-body) position operator expressed in this formalism reads

$$\hat{\mu} = \sum_{nm\mathbf{k}} \hat{a}_{n\mathbf{k}}^\dagger \hat{a}_{m\mathbf{k}} r_{nm\mathbf{k}}, \quad \text{where } r_{nm\mathbf{k}} = \langle n\mathbf{k} | \hat{\mathbf{r}} | m\mathbf{k} \rangle. \quad (\text{A2})$$

Using the definition of the excitonic state  $|\lambda\mathbf{q}\rangle$ , the matrix element (11) is written as

$$\begin{aligned} \langle \lambda\mathbf{q} | \hat{\mu} | g \rangle &= \sum_{c\nu\mathbf{k}} A_{c\nu\mathbf{k}}^{\lambda\mathbf{q}} \langle c\nu\mathbf{k} | \hat{\mu} | g \rangle, \\ \langle c\nu\mathbf{k} | \hat{\mu} | g \rangle &= \sum_{nm\mathbf{k}} \langle g | \hat{a}_{v\mathbf{k}}^\dagger \hat{a}_{c\mathbf{k}} \hat{a}_{n\mathbf{k}}^\dagger \hat{a}_{m\mathbf{k}} | g \rangle r_{nm\mathbf{k}}, \end{aligned} \quad (\text{A3})$$

and we have to remember that  $c$  is in the conduction sector,  $v$  is in the valence sector, and the sum over  $n$  and  $m$  is unrestricted. Looking at the bracket, we see that  $m$  has to be in the valence sector, otherwise  $\hat{a}_{m\mathbf{k}} | g \rangle = 0$ . The bracket is the scalar product of two states that is not zero only if  $m = v$  and  $n = c$ , so we obtain

$$\langle c\nu\mathbf{k} | \hat{\mu} | g \rangle = r_{c\nu\mathbf{k}}, \quad (\text{A4})$$

which is the expected result.

The definition of the position operator used here is ill-defined in periodic boundary conditions, in particular because the intraband terms are ill-defined. For systems with a gap this is not an issue in the derivation of Eq. (11) since only matrix elements with  $n$  in valence and  $m$  in conduction are involved. This problem will appear in the definition of the dipoles for exciton-to-exciton transitions, which will depend

on the term with  $n = m$ . One possible solution is to move from the length to the velocity gauge via the definition of the current operator  $j$ . Another involves the formal definition of  $r = \partial_{\mathbf{k}}$ . We do not explicitly address this issue in the present Appendix.

## 2. Nonequilibrium case: Exciton-to-exciton transitions

We now proceed with the derivation of Eq. (16). In the case of an initial state containing one exciton, three options can be considered for the final state for  $|J\rangle$ . (i)  $|F\rangle = |g\rangle$ , i.e., the probe stimulates the emission of a photon, back to the ground state. (ii)  $|F\rangle = |\lambda_i \mathbf{q}_i + \lambda_f \mathbf{q}_f\rangle$  with  $E_F = E_0 + \omega_{\lambda_i + \lambda_f}(\mathbf{q}_i + \mathbf{q}_f)$ , i.e., the probe stimulates the creation of a second exciton. The energy of the two-exciton (or biexciton) state can be in general lower than the sum of the two excitonic energies [ $\omega_{\lambda_i + \lambda_f}(\mathbf{q}_i + \mathbf{q}_f) < \omega_{\lambda_i}(\mathbf{q}_i) + \omega_{\lambda_f}(\mathbf{q}_f)$ ], due to the extra biexciton binding energy [74]. (iii)  $|F\rangle = |\lambda_f \mathbf{q}_f\rangle$  with  $E_F = E_0 + \omega_{\lambda_f}(\mathbf{q}_f)$ , i.e., the initial exciton is further excited into a different excitonic state. Due to the optical nature of the transition, we must have  $\mathbf{q}_i = \mathbf{q}_f$ . Omitting the momentum indexes and using  $\omega_\alpha = \omega_{\lambda_i + \lambda_f}$ , the expression for the response function has the form

$$\begin{aligned} \chi_{AB}(\omega) &= \frac{2}{V} \sum_f \frac{A_{\lambda_f} B_{f\lambda}^j}{E_f - E_\lambda - \omega - i\Gamma} = \frac{2}{V} \frac{A_{\lambda g} B_{g\lambda}}{-\omega_\lambda - \omega - i\Gamma} \\ &+ \frac{2}{V} \sum_\alpha \frac{A_{\lambda\alpha} B_{\alpha\lambda}}{\omega_\alpha - \omega_\lambda - \omega - i\Gamma} \\ &+ \frac{2}{V} \sum_{\lambda'} \frac{A_{\lambda\lambda'} B_{\lambda'\lambda}}{\omega'_{\lambda'} - \omega_\lambda - \omega - i\Gamma}. \end{aligned} \quad (\text{A5})$$

While in the first two cases (i) and (ii) peaks are expected in the energy range defined by  $\omega_\lambda(\mathbf{q})$ , we focus here on this latter case (iii), i.e., the last term in the equation, where peaks are expected at much lower energies.

We use the same approach of the previous section to derive a formula for the dipole matrix elements for exciton-to-exciton transitions. In this case, we have to deal with a matrix element of the form

$$\langle c\mathbf{v}\mathbf{k} | \hat{\mu} | c'\mathbf{v}'\mathbf{k} \rangle, \quad (\text{A6})$$

where  $c, c'$  are in the conduction sector, while  $v, v'$  are in the valence one. Plugging the expressions for excitonic states and position operator provides

$$\sum_{nm\mathbf{k}} \langle g | \hat{a}_{v\mathbf{k}}^\dagger \hat{a}_{c\mathbf{k}} \hat{a}_{n\mathbf{k}}^\dagger \hat{a}_{m\mathbf{k}} \hat{a}_{c'\mathbf{k}}^\dagger \hat{a}_{v'\mathbf{k}} | g \rangle r_{nm\mathbf{k}}. \quad (\text{A7})$$

We split the sum over  $n$  and  $m$  in the valence and conduction sector. We observe that if  $m$  is in conduction, we must have  $m = c'$ , while if  $n$  is in conduction, we must have  $n = c$ . Accordingly, we have four terms,

$$\begin{aligned} &\sum_{n,n \in \text{occ}, \mathbf{k}} \langle g | \hat{a}_{v\mathbf{k}}^\dagger \hat{a}_{c\mathbf{k}} \hat{a}_{n\mathbf{k}}^\dagger \hat{a}_{m\mathbf{k}} \hat{a}_{c'\mathbf{k}}^\dagger \hat{a}_{v'\mathbf{k}} | g \rangle r_{nm\mathbf{k}} \\ &+ \sum_{m \in \text{occ}, \mathbf{k}} \langle g | \hat{a}_{v\mathbf{k}}^\dagger \hat{a}_{m\mathbf{k}} \hat{a}_{c'\mathbf{k}}^\dagger \hat{a}_{v'\mathbf{k}} | g \rangle r_{cm\mathbf{k}} \end{aligned}$$

$$\begin{aligned} &+ \sum_{n \in \text{occ}, \mathbf{k}} \langle g | \hat{a}_{v\mathbf{k}}^\dagger \hat{a}_{c\mathbf{k}} \hat{a}_{n\mathbf{k}}^\dagger \hat{a}_{v'\mathbf{k}} | g \rangle r_{nc'\mathbf{k}} \\ &+ \langle g | \hat{a}_{v\mathbf{k}}^\dagger \hat{a}_{v'\mathbf{k}} | g \rangle r_{cc'\mathbf{k}}. \end{aligned}$$

Now we observe that the second term can be nonzero only if  $m = c'$  and the third if  $n = c$ , which are both nonallowed conditions because  $m$  and  $n$  are in the valence sector. So the expression reduces to

$$\sum_{n,m \in \text{occ}, \mathbf{k}} \langle g | \hat{a}_{v\mathbf{k}}^\dagger \hat{a}_{c\mathbf{k}} \hat{a}_{n\mathbf{k}}^\dagger \hat{a}_{m\mathbf{k}} \hat{a}_{c'\mathbf{k}}^\dagger \hat{a}_{v'\mathbf{k}} | g \rangle r_{nm\mathbf{k}} + \delta_{vv'} r_{cc'\mathbf{k}}.$$

We analyze the first bracket and we move  $\hat{a}_{v\mathbf{k}}^\dagger$  toward the right. This gives

$$\delta_{vm} \langle g | \hat{a}_{c\mathbf{k}} \hat{a}_{n\mathbf{k}}^\dagger \hat{a}_{c'\mathbf{k}}^\dagger \hat{a}_{v'\mathbf{k}} | g \rangle + \delta_{vv'} \langle g | \hat{a}_{c\mathbf{k}} \hat{a}_{n\mathbf{k}}^\dagger \hat{a}_{m\mathbf{k}} \hat{a}_{c'\mathbf{k}}^\dagger | g \rangle.$$

Now we observe that, in order to be nonzero, the ket and bra states have to be equal, so we match the indexes in the only way and we obtain

$$-\delta_{vm} \delta_{nv'} \delta_{cc'} + \delta_{vv'} \delta_{nm} \delta_{cc'}.$$

Putting everything together, we obtain

$$\langle c\mathbf{v}\mathbf{k} | \hat{\mu} | c'\mathbf{v}'\mathbf{k} \rangle = -\delta_{cc'} r_{v'\mathbf{v}\mathbf{k}} + \delta_{vv'} \delta_{cc'} \sum_{n \in \text{occ}} r_{nm\mathbf{k}} + \delta_{vv'} r_{cc'\mathbf{k}}. \quad (\text{A8})$$

Finally, we can insert this formula in the dipole matrix element of two excitonic states. This provides

$$\langle \lambda | \hat{\mu} | \lambda' \rangle = \sum_{c\mathbf{v}\mathbf{k}} \sum_{c'\mathbf{v}'\mathbf{k}} A_{c\mathbf{v}\mathbf{k}}^{\lambda*} A_{c'\mathbf{v}'\mathbf{k}}^{\lambda'} \langle c\mathbf{v}\mathbf{k} | \hat{\mu} | c'\mathbf{v}'\mathbf{k} \rangle,$$

and using (A8) we find

$$\begin{aligned} \langle \lambda | \hat{\mu} | \lambda' \rangle &= - \sum_{c\mathbf{v}\mathbf{k}} A_{c\mathbf{v}\mathbf{k}}^{\lambda*} A_{c'\mathbf{v}'\mathbf{k}}^{\lambda'} r_{v'\mathbf{v}\mathbf{k}} + \sum_{c\mathbf{v}\mathbf{k}} A_{c\mathbf{v}\mathbf{k}}^{\lambda*} A_{c'\mathbf{v}'\mathbf{k}}^{\lambda'} r_{cc'\mathbf{k}} \\ &+ \sum_{c\mathbf{v}\mathbf{k}} A_{c\mathbf{v}\mathbf{k}}^{\lambda*} A_{c'\mathbf{v}'\mathbf{k}}^{\lambda'} \sum_{n \in \text{occ}} r_{nm\mathbf{k}} \\ &= \sum_{v,c \neq c', \mathbf{k}} A_{c\mathbf{v}\mathbf{k}}^{\lambda*} A_{c'\mathbf{v}'\mathbf{k}}^{\lambda'} r_{cc'\mathbf{k}} - \sum_{c,v \neq v', \mathbf{k}} A_{c\mathbf{v}\mathbf{k}}^{\lambda*} A_{c'\mathbf{v}'\mathbf{k}}^{\lambda'} r_{v'\mathbf{v}\mathbf{k}} \\ &+ \sum_{v,c,\mathbf{k}} A_{c\mathbf{v}\mathbf{k}}^{\lambda*} A_{c'\mathbf{v}'\mathbf{k}}^{\lambda'} \left( r_{cc\mathbf{k}} - r_{vv\mathbf{k}} + \sum_{n \in \text{occ}} r_{nm\mathbf{k}} \right). \end{aligned} \quad (\text{A9})$$

A very similar expression was derived in Ref. [75], Eq. (B8), to model nonlinear optics in the independent-particles case. A similar expression is also derived in Ref. [76] (B3), apart from the last term.

## APPENDIX B: DIPOLE-ALLOWED TRANSITIONS BY SYMMETRY ANALYSIS

### 1. LiF bulk and the $O_h$ symmetry group

The point symmetry group of LiF is  $O_h$ , which has 48 symmetry operations and 10 irreducible representation (irreps), four of dimension 3 ( $T_{1u}, T_{2u}, T_{1g}, T_{2g}$ ), two of dimension 2 ( $E_u, E_g$ ), and four of dimension 1 ( $A_{1u}, A_{2u}, A_{1g}, A_{2g}$ ).

For the case of equilibrium absorption, the initial state corresponds to the ground state  $|\Psi_I\rangle = |\Psi_0\rangle$ , which is symmetric, thus  $O_I = A_{1g}$  irrep. The dipole operator instead  $\hat{\mu}$  belongs to

the  $T_{1u}$  irrep. Then, given the irreducible transformation  $O_F$  of the final state  $|\Psi_f\rangle$ , the integral is different from zero if the product of the symmetries gives  $A_{1g}$ , i.e.,

$$A_{1g} \in A_{1g} \times T_{1u} \times O_F. \quad (\text{B1})$$

To this end we need to look into the product table for the  $O_h$  group [63]. From the table, we see that  $A_{1g} \times T_{1u} = T_{1u}$  and the condition  $T_{1u} \times O_f = A_{1g}$  is verified only for

$$O_f = T_{1u}. \quad (\text{B2})$$

$T_{1u}$  has dimension 3, and  $\Psi_f$  is threefold-degenerate.

We move to the nonequilibrium case where the pump generates a bright excitonic state, thus  $O_I = T_{1u}$ . In this case, we need to perform the same exercise as before, looking for the states for which

$$A_{1g} \in T_{1u} \times T_{1u} \times O_F. \quad (\text{B3})$$

Since  $T_{1u} \times T_{1u} = A_{1g} + E_g + T_{1g} + T_{2g}$  and  $A_{1g} \in O_F \times O_F$ , we have that any

$$O_F = A_{1g}, E_g, T_{1g}, T_{2g} \quad (\text{B4})$$

is a possible solution. This already shows that the interexciton transition spectrum will show excitons that are dark when measuring absorption from equilibrium. Bright to bright transitions are not possible. A further push in the identification of the bright excitations can be achieved by analyzing also the relative polarization of the pump and probe pulses. Indeed, if both the pulses are parallel to (say) the  $z$ -direction, the associated irreps have to transform as the corresponding quadratic form of the coordinates, i.e., as  $z^2$  in this specific case. Then, the character table of  $O_h$  unambiguously identifies the first bright excitation (which is doubly degenerate) as  $E_g$  and the second one as  $A_{1g}$ . Instead for transverse polarization (with the probe parallel to the  $x$  axis), the allowed irreps have to transform as the bilinear product  $xz$ . This requirement is satisfied by both  $T_{2g}$ , which transforms as the quadratic form  $(xz, yz, xy)$ , and  $T_{1g}$ , which transforms as the rotation  $(R_x, R_y, R_z)$ . So in this case, this argument allows us to identify the two bright states as  $T_{1g}$  and  $T_{2g}$  excitons.

## 2. hBN monolayer and the $D(3h)$ symmetry group

For the case of the hBN monolayer, the point group is  $D_{3h}$ , which has six irreps:  $E'$  and  $E''$ , of dimension 2, and  $A'_1, A'_2, A''_1, A''_2$ , all of dimension 1. The ground state is symmetric and belongs to the  $A_1$  irrep.

The  $x$  and  $y$  components of the dipole operator, which are the relevant elements for the study of the in-plane excitation, belong to the  $E'$  irrep, while the  $z$  component belongs to  $A'_2$ . Following the same reasoning as for LiF, the in-plane optically active excitons belong to the  $E'$  irrep and are twofold-degenerate, while the out-of-plane optically active excitons belong to  $A'_2$ .

Moving to the nonequilibrium absorption, the initial configuration belongs to  $E'$  so the coupling with an in-plane dipole gives rise to  $(E' \times E') = (A'_1 + A'_2 + E')$ , i.e., it spans all the possible irreps in the *primed sector* of the point group. So, any exciton in this sector can be reached measuring absorption from an optical excited state, inde-

pendently of the fact that the exciton is bright or dark at equilibrium.

Also in this case, the polarization-based analysis allows us to discriminate the representation to which the bright states belong. Indeed, for pulses both parallel to (say) the  $x$ -axis, the excited states transform as the  $x^2$  quadratic form, so only  $E'$  (with a double degeneracy) and  $A'_1$  (nondegenerate) are allowed. On the contrary, for transverse in-plane polarization, the excited state transforms as the bilinear  $xy$ , so only  $E'$  and  $A'_2$  (that transforms as the  $R_z$  rotation) are allowed.

## APPENDIX C: SELECTION OF THE DEGENERATE EXCITONIC STATE

In the presence of degenerate bright excitons, we select, in the degenerate excitonic space  $U_d^i$ , the specific linear combination of states that gives an excitonic transition dipole along the direction of the pump laser pulse  $\mathcal{E}_0$ . To this end, we define a “dipoles matrix” and a “directions matrix”:

$$D_{\alpha\lambda} = \frac{\mu_{0\lambda}^\alpha(\mathbf{0})}{|\mu_{0\lambda}(\mathbf{0})|}, \quad (\text{C1})$$

$$E_{\alpha n} = \frac{\mathcal{E}_n^\alpha}{|\mathcal{E}_n|}. \quad (\text{C2})$$

These two matrices are  $n_{\text{deg}} \times n_{\text{deg}}$ , depending on the size of the degenerate space. For LiF,  $n_{\text{deg}} = 3$ , and the transition dipoles of the three states span the whole space. For hBN,  $n_{\text{deg}} = 2$ , and the transition dipoles span the  $xy$  plane. Here  $\lambda$  are the indexes of the exciton in  $U_d^i$ , while  $n$  runs from 0 to  $n_{\text{deg}} - 1$ .  $\mathcal{E}_n$ , with  $n > 0$ , are directions orthogonal to  $\mathcal{E}_0$  that belong to the space spanned by the transition dipoles. Thanks to these two matrices, we can define the rotation matrix

$$C_{\lambda n} = \sum_{\alpha} D_{\lambda\alpha}^i E_{\alpha n}. \quad (\text{C3})$$

$C_{\lambda 0}$  is used to construct the excitonic states

$$|\lambda_n\rangle = \sum_{\lambda} C_{\lambda 0} |\lambda\rangle. \quad (\text{C4})$$

The states  $|\lambda_n\rangle$  span the same space spanned by the random vectors  $|\lambda\rangle$ , but now the initial state  $|\lambda_i\rangle = |\lambda_0\rangle$  has polarization parallel to  $E_{\alpha 0}$ .

## APPENDIX D: INTRABAND TERM: POSITION VERSUS VELOCITY DIPOLES

Intraband dipoles  $r_{nm\mathbf{k}}$  are ill-defined in the length gauge. They can instead be accounted for within the velocity gauge and thus shifting to the (one-body) velocity dipole matrix elements  $\mathbf{v}_{nm\mathbf{k}}^{1b}$ . In the linear regime starting from a nonequilibrium state, position and velocity dipoles can be related by the expression

$$\mathbf{v}_{nm\mathbf{k}}^{1b} = i \mathbf{r}_{nm\mathbf{k}} \Delta \epsilon_{nm\mathbf{k}} + \delta_{n,m} \partial_{\mathbf{k}} \epsilon_{n\mathbf{k}}. \quad (\text{D1})$$

The above equation can be found in many works in the literature [77] for the case  $\Delta \epsilon_{nm\mathbf{k}} > 0$ , while the expression for the terms with  $n = m$  can be obtained by the expression



for the energies in the  $\mathbf{k} \cdot \mathbf{v}$  model [78] in the presence of nondegenerate bands:  $\epsilon_{n\mathbf{k}+\mathbf{q}} \simeq \epsilon_{n\mathbf{k}} + \mathbf{q} \cdot \mathbf{v}_{n\mathbf{k}}$ .

Notice that such an equation also shows that the physics of intraband transitions enters differently in the two gauges. Indeed, while for  $\Delta\epsilon_{nm\mathbf{k}} > 0$  the two dipoles carry the same information, for  $n = m$  the velocity dipoles carry extra information which cannot be obtained from the length dipoles alone. However, while the velocity dipoles capture the physics of intraband transitions, their use within the velocity gauge has two main drawbacks: (i) sum rules are easily broken in numerical implementations, and (ii) beyond the independent-particles approximation the definition of the velocity operator depends on the Hamiltonian [60].

### APPENDIX E: APPROXIMATED HSEX SELF-ENERGY

The  $\Delta\Sigma^{\text{HSEX}}[\rho(t)]$  appearing in Eq. (2) is calculated in the YAMBO code as [40]

$$\Delta\Sigma_{mm'\mathbf{k}}^{\text{HSEX}}(t) = \sum_{n,n'\mathbf{q}} M_{mm'\mathbf{q}} \cdot \Delta\rho_{n,n'\mathbf{k}-\mathbf{q}}(t), \quad (\text{E1})$$

where the matrix elements of  $M$  are defined as the sum of two terms:

$$M_{mm'\mathbf{k}}^{\text{H}} = \sum_{\mathbf{G}} \rho_{mm'\mathbf{k}}^{\mathbf{G}}(\mathbf{0}) [\rho_{m'n'\mathbf{k}-\mathbf{q}}^{\mathbf{G}}(\mathbf{0})]^* v_{\mathbf{G}}(\mathbf{q}), \quad (\text{E2})$$

$$M_{mm'\mathbf{k}}^{\text{SEX}} = \sum_{\mathbf{G},\mathbf{G}'} \rho_{mm'\mathbf{k}}^{\mathbf{G}'}(\mathbf{q}) [\rho_{m'n'\mathbf{k}}^{\mathbf{G}}(\mathbf{q})]^* W_{\mathbf{G},\mathbf{G}'}(\mathbf{q}), \quad (\text{E3})$$

where

$$\rho_{mn\mathbf{k}}(\mathbf{q}, \mathbf{G}) = \int \varphi_{m\mathbf{k}}^*(\mathbf{r}) \varphi_{n\mathbf{k}-\mathbf{q}}(\mathbf{r}) e^{i(\mathbf{G}+\mathbf{q})\mathbf{r}}. \quad (\text{E4})$$

$v$  and  $W$  are the bare and the screened Coulomb interaction already introduced in the main text [79]. In this work, we considered only matrix elements of  $M$  involving both  $m, n$  in the valence (conduction) when  $m', n'$  are both in the conduction (valence) band. Instead, we set to zero all elements where either  $m, m'$  or  $n, n'$  are both in the conduction (valence) band. This approximation strongly reduces the computational cost, it is exact for the linear response, and we verified that it does not introduce any relevant change in the pump and probe spectra reported in the main text.

- 
- [1] Y. Toyozawa and C. Oxlade, *Optical Processes in Solids* (Cambridge University Press, 2003).
- [2] K. S. Thygesen, Calculating excitons, plasmons, and quasiparticles in 2D materials and van der waals heterostructures, *2D Mater.* **4**, 022004 (2017).
- [3] L. X. Benedict, E. L. Shirley, and R. B. Bohn, Optical Absorption of Insulators and the Electron-Hole Interaction: An *Ab Initio* Calculation, *Phys. Rev. Lett.* **80**, 4514 (1998).
- [4] M. Rohlfing and S. G. Louie, Electron-Hole Excitations in Semiconductors and Insulators, *Phys. Rev. Lett.* **81**, 2312 (1998).
- [5] M. Rohlfing and S. G. Louie, Electron-hole excitations and optical spectra from first principles, *Phys. Rev. B* **62**, 4927 (2000).
- [6] Y. Kubota, K. Watanabe, O. Tsuda, and T. Taniguchi, Deep ultraviolet light-emitting hexagonal boron nitride synthesized at atmospheric pressure, *Science* **317**, 932 (2007).
- [7] T. Galvani, F. Paleari, H. P. C. Miranda, A. Molina-Sánchez, L. Wirtz, S. Latil, H. Amara, and F. Ducastelle, Excitons in boron nitride single layer, *Phys. Rev. B* **94**, 125303 (2016).
- [8] T. Kazimierzczuk, D. Fröhlich, S. Scheel, H. Stolz, and M. Bayer, Giant rydberg excitons in the copper oxide  $\text{Cu}_2\text{O}$ , *Nature (London)* **514**, 343 (2014).
- [9] Y. Kaifu, Excitons in layered  $\text{BiI}_3$  single crystals, *J. Lumin.* **42**, 61 (1988).
- [10] S. Mor, V. Gosetti, A. Molina-Sánchez, D. Sangalli, S. Achilli, V. F. Agekyan, P. Franceschini, C. Giannetti, L. Sangaletti, and S. Pagliara, Photoinduced modulation of the excitonic resonance via coupling with coherent phonons in a layered semiconductor, *Phys. Rev. Res.* **3**, 043175 (2021).
- [11] A. A. Bakulin, A. Rao, V. G. Pavelyev, P. H. M. van Loosdrecht, M. S. Pshenichnikov, D. Niedzialek, J. Cornil, D. Beljonne, and R. H. Friend, The role of driving energy and delocalized states for charge separation in organic semiconductors, *Science* **335**, 1340 (2012).
- [12] S. Gélinas, O. Paré-Labrosse, C.-N. Brosseau, S. Albert-Seifried, C. R. McNeill, K. R. Kirov, I. A. Howard, R. Leonelli, R. H. Friend, and C. Silva, The binding energy of charge-transfer excitons localized at polymeric semiconductor heterojunctions, *J. Phys. Chem. C* **115**, 7114 (2011).
- [13] T. Mueller and E. Malic, Exciton physics and device application of two-dimensional transition metal dichalcogenide semiconductors, *npj 2D Mater. Appl.* **2**, 1 (2018).
- [14] M. Selig, F. Katsch, R. Schmidt, S. M. de Vasconcellos, R. Bratschitsch, E. Malic, and A. Knorr, Ultrafast dynamics in monolayer transition metal dichalcogenides: interplay of dark excitons, phonons, and intervalley exchange, *Phys. Rev. Res.* **1**, 022007(R) (2019).
- [15] F. Paleari, H. P. C. Miranda, A. Molina-Sánchez, and L. Wirtz, Exciton-Phonon Coupling in the Ultraviolet Absorption and Emission Spectra of Bulk Hexagonal Boron Nitride, *Phys. Rev. Lett.* **122**, 187401 (2019).
- [16] P. Lechiffart, F. Paleari, D. Sangalli, and C. Attaccalite, First-principles study of luminescence in hexagonal boron nitride single layer: Exciton-phonon coupling and the role of substrate, *Phys. Rev. Mater.* **7**, 024006 (2023).
- [17] H.-Y. Chen, D. Sangalli, and M. Bernardi, Exciton-Phonon Interaction and Relaxation Times from First Principles, *Phys. Rev. Lett.* **125**, 107401 (2020).
- [18] G. Antonius and S. G. Louie, Theory of exciton-phonon coupling, *Phys. Rev. B* **105**, 085111 (2022).
- [19] H.-Y. Chen, D. Sangalli, and M. Bernardi, First-principles ultrafast exciton dynamics and time-domain spectroscopies: Dark-exciton mediated valley depolarization in monolayer  $\text{WSe}_2$ , *Phys. Rev. Res.* **4**, 043203 (2022).
- [20] E. Peretto, D. Sangalli, A. Marini, and G. Stefanucci, Pump-driven normal-to-excitonic insulator transition: Josephson

- oscillations and signatures of BEC-BCS crossover in time-resolved arpes, *Phys. Rev. Mater.* **3**, 124601 (2019).
- [21] D. Sangalli, Excitons and carriers in transient absorption and time-resolved arpes spectroscopy: An ab initio approach, *Phys. Rev. Mater.* **5**, 083803 (2021).
- [22] S. Dong, M. Puppini, T. Pincelli, S. Beaulieu, D. Christiansen, H. Hübener, C. W. Nicholson, R. P. Xian, M. Dendzik, Y. Deng, Y. W. Windsor, M. Selig, E. Malic, A. Rubio, A. Knorr, M. Wolf, L. Rettig, and R. Ernstorfer, Direct measurement of key exciton properties: Energy, dynamics, and spatial distribution of the wave function, *Nat. Sci.* **1**, e10010 (2021).
- [23] M. K. L. Man, J. Madéo, C. Sahoo, K. Xie, M. Campbell, V. Pareek, A. Karmakar, E. L. Wong, A. Al-Mahboob, N. S. Chan, D. R. Bacon, X. Zhu, M. M. M. Abdelrasoul, X. Li, T. F. Heinz, F. H. da Jornada, T. Cao, and K. M. Dani, Experimental measurement of the intrinsic excitonic wave function, *Sci. Adv.* **7**, eabg0192 (2021).
- [24] G. Cassabois, P. Valvin, and B. Gil, Hexagonal boron nitride is an indirect bandgap semiconductor, *Nat. Photon.* **10**, 262 (2016).
- [25] Z. Ye, T. Cao, K. O'Brien, H. Zhu, X. Yin, Y. Wang, S. G. Louie, and X. Zhang, Probing excitonic dark states in single-layer tungsten disulphide, *Nature (London)* **513**, 214 (2014).
- [26] D. Panna, K. Balasubramanian, J. Khatei, L. Rybak, Y. Slobodkin, H. Steinberg, and A. Hayat, Observation of 2D semiconductor P-type dark-exciton lifetime using two-photon ultrafast spectroscopy, *Opt. Express* **27**, 33427 (2019).
- [27] F. Wang, G. Dukovic, L. E. Brus, and T. F. Heinz, The optical resonances in carbon nanotubes arise from excitons, *Science* **308**, 838 (2005).
- [28] C. Attaccalite, M. Grüning, H. Amara, S. Latil, and F. Ducastelle, Two-photon absorption in two-dimensional materials: The case of hexagonal boron nitride, *Phys. Rev. B* **98**, 165126 (2018).
- [29] R. Huber, R. A. Kaindl, B. A. Schmid, and D. S. Chemla, Broadband terahertz study of excitonic resonances in the high-density regime in GaAs/Al<sub>x</sub>Ga<sub>1-x</sub>As quantum wells, *Phys. Rev. B* **72**, 161314(R) (2005).
- [30] R. A. Kaindl, M. A. Carnahan, D. Hägele, R. Lövenich, and D. S. Chemla, Ultrafast terahertz probes of transient conducting and insulating phases in an electron-hole gas, *Nature (London)* **423**, 734 (2003).
- [31] T. Suzuki and R. Shimano, Time-Resolved Formation of Excitons and Electron-Hole Droplets in Si Studied Using Terahertz Spectroscopy, *Phys. Rev. Lett.* **103**, 057401 (2009).
- [32] T. Suzuki and R. Shimano, Exciton Mott Transition in Si Revealed by Terahertz Spectroscopy, *Phys. Rev. Lett.* **109**, 046402 (2012).
- [33] M. Jörger, T. Fleck, C. Klingshirn, and R. von Baltz, Midinfrared properties of cuprous oxide: High-order lattice vibrations and intraexcitonic transitions of the 1s paraexciton, *Phys. Rev. B* **71**, 235210 (2005).
- [34] C. Poellmann, P. Steinleitner, U. Leierseder, P. Nagler, G. Plechinger, M. Porer, R. Bratschitsch, C. Schüller, T. Korn, and R. Huber, Resonant internal quantum transitions and femtosecond radiative decay of excitons in monolayer WSe<sub>2</sub>, *Nat. Mater.* **14**, 889 (2015).
- [35] S. Cha, J. H. Sung, S. Sim, J. Park, H. Heo, M.-H. Jo, and H. Choi, 1s-intraexcitonic dynamics in monolayer MoS<sub>2</sub> probed by ultrafast mid-infrared spectroscopy, *Nat. Commun.* **7**, 10768 (2016).
- [36] P. Steinleitner, P. Merkl, A. Graf, P. Nagler, K. Watanabe, T. Taniguchi, J. Zipfel, C. Schüller, T. Korn, A. Chernikov, S. Brem, M. Selig, G. Berghäuser, E. Malic, and R. Huber, Dielectric engineering of electronic correlations in a van der waals heterostructure, *Nano Lett.* **18**, 1402 (2018).
- [37] P. Merkl, F. Mooshammer, P. Steinleitner, A. Girnguber, K.-Q. Lin, P. Nagler, J. Holler, C. Schüller, J. M. Lupton, T. Korn, S. Ovesen, S. Brem, E. Malic, and R. Huber, Ultrafast transition between exciton phases in van der waals heterostructures, *Nat. Mater.* **18**, 691 (2019).
- [38] L. Luo, L. Men, Z. Liu, Y. Mudryk, X. Zhao, Y. Yao, J. M. Park, R. Shinar, J. Shinar, K.-M. Ho, I. E. Perakis, J. Vela, and J. Wang, Ultrafast terahertz snapshots of excitonic rydberg states and electronic coherence in an organometal halide perovskite, *Nat. Commun.* **8**, 15565 (2017).
- [39] K. S. Virk and J. E. Sipe, Multidimensional fourier spectroscopy of semiconductors. I. nonequilibrium green function approach, *Phys. Rev. B* **80**, 165318 (2009).
- [40] C. Attaccalite, M. Grüning, and A. Marini, Real-time approach to the optical properties of solids and nanostructures: Time-dependent bethe-salpeter equation, *Phys. Rev. B* **84**, 245110 (2011).
- [41] C. Attaccalite and M. Grüning, Nonlinear optics from an *ab initio* approach by means of the dynamical berry phase: Application to second- and third-harmonic generation in semiconductors, *Phys. Rev. B* **88**, 235113 (2013).
- [42] I. Souza, J. Íñiguez, and D. Vanderbilt, Dynamics of berry-phase polarization in time-dependent electric fields, *Phys. Rev. B* **69**, 085106 (2004).
- [43] G. Strinati, Application of the green's functions method to the study of the optical properties of semiconductors, *Riv. Nuovo Cim.* **11**, 1 (1988).
- [44] A. Riefer and W. G. Schmidt, Solving the bethe-salpeter equation for the second-harmonic generation in Zn chalcogenides, *Phys. Rev. B* **96**, 235206 (2017).
- [45] E. L. Shirley, L. J. Terminello, J. E. Klepeis, and F. J. Himpsel, Detailed theoretical photoelectron angular distributions for LiF(100), *Phys. Rev. B* **53**, 10296 (1996).
- [46] P. Puschnig and C. Ambrosch-Draxl, Optical absorption spectra of semiconductors and insulators including electron-hole correlations: An ab initio study within the lapw method, *Phys. Rev. B* **66**, 165105 (2002).
- [47] N.-P. Wang, M. Rohlfiing, P. Krüger, and J. Pollmann, Quasi-particle band structure and optical spectrum of LiF(001), *Phys. Rev. B* **67**, 115111 (2003).
- [48] A. Marini, R. Del Sole, and A. Rubio, Bound Excitons in Time-Dependent Density-Functional Theory: Optical and Energy-Loss Spectra, *Phys. Rev. Lett.* **91**, 256402 (2003).
- [49] P. Abbamonte, T. Graber, J. P. Reed, S. Smadici, C.-L. Yeh, A. Shukla, J.-P. Rueff, and W. Ku, Dynamical reconstruction of the exciton in LiF with inelastic x-ray scattering, *Proc. Natl. Acad. Sci. (USA)* **105**, 12159 (2008).
- [50] W. Olovsson, I. Tanaka, P. Puschnig, and C. Ambrosch-Draxl, Near-edge structures from first principles all-electron bethe-salpeter equation calculations, *J. Phys.: Condens. Matter* **21**, 104205 (2009).
- [51] C.-C. Lee, X. M. Chen, Y. Gan, C.-L. Yeh, H. C. Hsueh, P. Abbamonte, and W. Ku, First-Principles Method of Propagation

- of Tightly Bound Excitons: Verifying the Exciton Band Structure of LiF with Inelastic x-Ray Scattering, *Phys. Rev. Lett.* **111**, 157401 (2013).
- [52] M. Gatti and F. Sottile, Exciton dispersion from first principles, *Phys. Rev. B* **88**, 155113 (2013).
- [53] L. Schué, L. Sponza, A. Plaud, H. Bensalah, K. Watanabe, T. Taniguchi, F. Ducastelle, A. Loiseau, and J. Barjon, Bright Luminescence from Indirect and Strongly Bound Excitons in *h*-BN, *Phys. Rev. Lett.* **122**, 067401 (2019).
- [54] W. Kohn and L. J. Sham, Self-consistent equations including exchange and correlation effects, *Phys. Rev.* **140**, A1133 (1965).
- [55] D. Sangalli, A. Ferretti, H. Miranda, C. Attaccalite, I. Marri, E. Cannuccia, P. Melo, M. Marsili, F. Paleari, A. Marrazzo, G. Prandini, P. Bonfà, M. O. Atambo, F. Affinito, M. Palumbo, A. Molina-Sánchez, C. Hogan, M. Grüning, D. Varsano, and A. Marini, Many-body perturbation theory calculations using the yambo code, *J. Phys.: Condens. Matter* **31**, 325902 (2019).
- [56] R. W. Nunes and X. Gonze, Berry-phase treatment of the homogeneous electric field perturbation in insulators, *Phys. Rev. B* **63**, 155107 (2001).
- [57] T. Otake, Y. Shinohara, S. A. Sato, and K. Yabana, Femtosecond time-resolved dynamical Franz-Keldysh effect, *Phys. Rev. B* **93**, 045124 (2016).
- [58] E. Perfetto, D. Sangalli, A. Marini, and G. Stefanucci, Nonequilibrium bethe-salpeter equation for transient photoabsorption spectroscopy, *Phys. Rev. B* **92**, 205304 (2015).
- [59] S.-L. Chuang, S. Schmitt-Rink, D. A. B. Miller, and D. S. Chemla, Exciton green's-function approach to optical absorption in a quantum well with an applied electric field, *Phys. Rev. B* **43**, 1500 (1991).
- [60] D. Sangalli, J. A. Berger, C. Attaccalite, M. Grüning, and P. Romaniello, Optical properties of periodic systems within the current-current response framework: Pitfalls and remedies, *Phys. Rev. B* **95**, 155203 (2017).
- [61] Here  $\mathbf{q}$  is the momentum of the final state, while we are interested in optical transitions only, i.e., zero transferred momentum  $\mathbf{Q}$ . Different operators can be used to define transitions with finite momentum transfer in the length and in the velocity gauge, namely  $e^{i\mathbf{Q}\cdot\mathbf{r}}$  and  $\hat{v}e^{i\mathbf{Q}\cdot\mathbf{r}}$ . We do not discuss these transitions here.
- [62] While the formulation in terms of real-time propagation can account for these effects, a full formulation in terms of the response function could also be achieved within equilibrium MBPT formalism. This would require us to apply MBPT starting from a noninteracting excited state [20]. This, however, leads to problems, since the formalism would rely on the use of the adiabatic connection for excited states.
- [63] M. S. Dresselhaus, G. Dresselhaus, and A. Jorio, *Group Theory: Application to the Physics of Condensed Matter* (Springer-Verlag, Berlin, 2008).
- [64] H. Tatewaki and E. Miyoshi, The surface and bulk excitons of crystalline LiF.  $\text{Li}_n^+ \text{F}_m^-$  cluster embedded in an ionic cage, *Surf. Sci.* **327**, 129 (1995).
- [65] D. Sangalli, S. Dal Conte, C. Manzoni, G. Cerullo, and A. Marini, Nonequilibrium optical properties in semiconductors from first principles: A combined theoretical and experimental study of bulk silicon, *Phys. Rev. B* **93**, 195205 (2016).
- [66] C. Trovatiello, F. Katsch, Q. Li, X. Zhu, A. Knorr, G. Cerullo, and S. Dal Conte, Disentangling many-body effects in the coherent optical response of 2D semiconductors, *Nano Lett.* **22**, 5322 (2022).
- [67] D. Snoke, Predicting the ionization threshold for carriers in excited semiconductors, *Solid State Commun.* **146**, 73 (2008).
- [68] A. Rousseau, L. Ren, A. Durand, P. Valvin, B. Gil, K. Watanabe, T. Taniguchi, B. Urbaszek, X. Marie, C. Robert *et al.*, Monolayer boron nitride: Hyperspectral imaging in the deep ultraviolet, *Nano Lett.* **21**, 10133 (2021).
- [69] For a 2D material we define the effective imaginary part of the dielectric constant as the 2D polarizability per surface unit  $\alpha^{2D}$  divided by an effecting distance along the  $z$  direction. For hBN we used  $L_{\text{eff}} = 3.25 \text{ \AA}$ ,  $\epsilon_2^{\text{eff}}(\omega) = \text{Im}[\alpha^{2D}(\omega)]/L_{\text{eff}}$ .
- [70] F. Zhang, C. S. Ong, J. W. Ruan, M. Wu, X. Q. Shi, Z. K. Tang, and S. G. Louie, Intervalley Excitonic Hybridization, Optical Selection Rules, and Imperfect Circular Dichroism in Monolayer *h*-BN, *Phys. Rev. Lett.* **128**, 047402 (2022).
- [71] L. Artús, M. Feneberg, C. Attaccalite, J. H. Edgar, J. Li, R. Goldhahn, and R. Cuscó, Ellipsometry study of hexagonal boron nitride using synchrotron radiation: Transparency window in the Far-UVC, *Adv. Photon. Res.* **2**, 2000101 (2021).
- [72] F. Bruneval and X. Gonze, Accurate *GW* self-energies in a plane-wave basis using only a few empty states: Towards large systems, *Phys. Rev. B* **78**, 085125 (2008).
- [73] Notice that in the real-time calculations, we included interactions only between valence and conduction bands [40]. We verified that this approximation does not affect the final spectra; see Appendix E.
- [74] W. Schäfer and M. Wegener, *Semiconductor Optics and Transport Phenomena* (Springer Science & Business Media, 2013).
- [75] R. Leitsmann, W. G. Schmidt, P. H. Hahn, and F. Bechstedt, Second-harmonic polarizability including electron-hole attraction from band-structure theory, *Phys. Rev. B* **71**, 195209 (2005).
- [76] A. Taghizadeh and T. G. Pedersen, Gauge invariance of excitonic linear and nonlinear optical response, *Phys. Rev. B* **97**, 205432 (2018).
- [77] K. S. Virk and J. E. Sipe, Semiconductor optics in length gauge: A general numerical approach, *Phys. Rev. B* **76**, 035213 (2007).
- [78] E. Luppi, H. Hübener, and V. Véniard, Ab initio second-order nonlinear optics in solids: Second-harmonic generation spectroscopy from time-dependent density-functional theory, *Phys. Rev. B* **82**, 235201 (2010).
- [79] F. Aryasetiawan and O. Gunnarsson, The *GW* method, *Rep. Prog. Phys.* **61**, 237 (1998).